Ablation of Proton/Glucose Exporter *SLC45A2* Enhances Melanosomal Glycolysis to Inhibit Melanin Biosynthesis and Promote Melanoma Metastasis

JIDOpen

Ye Liu[1,7], Wenna Chi[1,2,7], Lei Tao[1,2], Guoqiang Wang[1], R.N.V. Krishna Deepak[3], Linlin Sheng[1], Taiqi Chen[4], Yaqian Feng[1], Xizhi Cao[1], Lili Cheng[1], Xinbin Zhao[1], Xiaohui Liu[5], Haiteng Deng[5], Hao Fan[3], Peng Jiang[4] and Ligong Chen[1,2]

Sequence variation in *SLC45A2* are responsible for oculocutaneous albinism type 4 in many species and are associated with melanoma susceptibility, but the molecular mechanism is unclear. In this study, we used *Slc45a2*-deficient melanocyte and mouse models to elucidate the roles of SLC45A2 in melanogenesis and melanoma metastasis. We found that the acidified cellular environment impairs the activity of key melanogenic enzyme tyrosinase in *Slc45a2*-deficient melanocytes. SLC45A2 is identified as a proton/glucose exporter in melanosomes, and its ablation increases the acidification of melanosomal pH through enhanced glycolysis. Intriguingly, ^{13}C-glucose-labeled metabolic flux and biochemical assays show that melanosomes are active glucose-metabolizing organelles, indicating that elevated glycolysis mainly occurs in melanosomes owing to *Slc45a2* deficiency. Moreover, *Slc45a2* deficiency significantly upregulates the activities of glycolytic enzymes and phosphatidylinositol 3-kinase/protein kinase B signaling to promote glycolysis-dependent survival and metastasis of melanoma cells. Collectively, our study reveals that the proton/glucose exporter SLC45A2 mediates melanin synthesis and melanoma metastasis primarily by modulating melanosomal glucose metabolism.

Journal of Investigative Dermatology (2022) ■, ■−■; doi:10.1016/j.jid.2022.04.008

INTRODUCTION

Solute carrier transporters are the second largest family of membrane proteins responsible for the transport of various substances such as saccharides, lipids, amino acids, and inorganic ions across cellular membranes (Zhang et al., 2019). One third of all solute carriers such as SLC2, SLC22, and SLC45 subfamily belong to the major facilitator superfamily clan (Chen et al., 2014; Perland et al., 2017). The majority of major facilitator superfamily proteins are generated from a single two-transmembrane segment hairpin structure that triplicated to give a six two-transmembrane segment unit and then duplicated to a 12-two-transmembrane segment protein (Reddy et al., 2012). The most widely accepted working model for transporters is the alternating access mechanism with alternated facilitated access to binding sites on either side of the membrane (Diallinas, 2014).

Multiple membrane proteins, including pumps, channels, and transporters, are involved in melanosome biogenesis in melanocytes. Sodium ion/potassium ion/calcium ion exchanger SLC24A5 is specifically expressed in pigmented tissues, and loss of SLC24A5 activity causes oculocutaneous albinism type 6 in human (Wei et al., 2013). SLC9A3 and SLC9A7 are sodium ion/proton (H^+) exchangers that colocalized with melanosome marker TYRP1 to regulate melanosome pH (Smith et al., 2004). Cystine/glutamate exchanger SLC7A11 is essential to pheomelanin production and regulates tyrosinase (TYR) transport in melanocytes (Chintala et al., 2005). SLC7A5 has been recently reported to affect melanogenesis in B16F10 cells (Gaudel et al., 2020). Sequence alteration in the *CTNS* gene that encodes a cystine/H^+ symporter leads to cystinosis, and in vitro studies have shown that CTNS was located at melanosomes in pigment cells to regulate melanogenesis (Chiaverini et al., 2012). As an atypical solute carrier of major facilitator superfamily type, cysteine exporter MFSD12, which is localized at melanosomes or lysosomes (Adelmann et al., 2020), is associated with skin pigmentation in African populations (Crawford et al.,). Therefore, functional disruptions of many solute carrier transporters are known to cause pigmentary disorders.

[1]*School of Pharmaceutical Sciences, MOE Key Laboratory of Bioorganic Phosphorus Chemistry & Chemical Biology, Tsinghua University, Beijing, China;* [2]*Collaborative Innovation Center for Biotherapy, State Key Laboratory of Biotherapy and Cancer Center, West China Hospital, West China Medical School, Sichuan University, Chengdu, China;* [3]*Bioinformatics Institute (BII), Agency for Science, Technology and Research (A*STAR), Singapore, Singapore;* [4]*School of Life Sciences, Tsinghua University, Beijing, China; and* [5]*National Center for Protein Science, School of Life Sciences, Tsinghua University, Beijing, China*

[7]*These authors contributed equally to this work.*

Correspondence: Ligong Chen, School of Pharmaceutical Sciences, Tsinghua University, Beijing 100084, China. E-mail: ligongchen@tsinghua.edu.cn

Abbreviations: Akt, protein kinase B; H^+, proton; HG, high glucose; HK, hexokinase; KO, knockout; LDHA, lactate dehydrogenase A; LG, low glucose; MMP, matrix metalloproteinase; MS, mass spectrometry; PI3K, phosphatidylinositol 3-kinase; PMC, primary melanocyte; Tyr, tyrosinase; WT, wild type

Received 30 November 2021; revised 11 March 2022; accepted 11 April 2022; accepted manuscript published online XXX; corrected proof published online XXX

© 2022 The Authors. Published by Elsevier, Inc. on behalf of the Society for Investigative Dermatology. This is an open access article under the CC BY-NC-ND license (http://creativecommons.org/licenses/by-nc-nd/4.0/).

SLC45A2 is the known pathogenic gene of an autosomal recessive hypopigmentary disorder oculocutaneous albinism type 4 (Inagaki et al., 2006) with >70 single-nucleotide variation, or frameshifts of *SLC45A2* have been recorded in oculocutaneous albinism type 4 database. Moreover, SLC45A2 variants show a strong association with the risk for melanoma. Two nonpathogenic *SLC45A2* variants (p. F374L and p. E272K) are associated with dark skin color and have strong protective effects in light-skinned population for malignant melanoma (Fernandez et al., 2008; Guedj et al., 2008). Another study indicates that SLC45A2 could be a promising immunotherapeutic target for melanoma with high tumor selectivity and reduced autoimmune toxicity (Park et al., 2017a).

The sugar transport activity of SLC45A2 in yeast cells shows an acid-dependent sugar transport mechanism (Bartölke et al., 2014). However, the transport mechanism of SLC45A2 is controversial. SLC45A2 was proposed to export H^+ and sucrose from the organelle to the cytosol (Le et al., 2020) or import sucrose and H^+ into melanosomes for osmotic compensation (Vitavska and Wieczorek, 2013). Therefore, SLC45A2 substrate and mechanism causing oculocutaneous albinism type 4 remain to be defined.

Sugar and sugar derivatives are shown to have antimelanogenic effects on melanocytes, probably through three different mechanisms: increasing melanosomal pH, disturbing melanosome maturation, and inhibiting TYR maturation by blocking *N*-glycosylation (Bin et al., 2016). As the main source of cellular energy, glucose is metabolized to lactate through glycolysis, which leads to cellular acidosis and then indirectly inhibits TYR activity (Lee et al., 2020). Therefore, glucose metabolism may be closely involved in pigmentation.

In this study, we characterized SLC45A2 essential functions in melanogenesis and melanoma development. SLC45A2 deficiency increased glycolysis and promoted glycolytic enzyme activities in melanosomes. Furthermore, overactive glycolysis in *SLC45A2* knockout (KO) promoted cell survival under glucose starvation and accelerated melanoma metastasis. Therefore, our results shed light on a glucose metabolic regulation of SLC45A2, which suggests, to our knowledge, a previously unreported therapeutic strategy for treating pigmentary disorders.

RESULTS

SLC45A2 mediates melanogenesis by regulating TYR activity and physically interacting with TYRP1

Slc45a2 mRNA levels were highly enriched in the eyes and primary melanocytes (PMCs) isolated from the murine epidermis (Supplementary Figure S1a). To assess the role of *Slc45a2* in pigmentation, we established a *Slc45a2*-deficient (KO) mouse model with CRISPR/Cas9 (Supplementary Figure S1b and c). Compared with wild-type (WT) mice, the *Slc45a2*-KO mice had clear white fur (Figure 1a) and red and transparent eyes without melanin in the retinal pigment epithelium and choroid (Figure 1b). Genetic KO of *Slc45a2* led to nearly complete loss of melanin in both melanocytes and culture media (Figure 1c-e and Supplementary Figure S1d). Noting that the murine melanoma cell line B16F10 expresses *Slc45a2* at a relatively high level (Supplementary Figure S1e), we then generated *Slc45a2*-KO B16F10 cell line (Supplementary Figure S1f), which also showed clear hypopigmentation phenotype (Figure 1e).

The protein level and three glycosylation peptides of TYR were slightly decreased in KO PMC compared with those in WT (Figure 1f and Supplementary Figure S1g and h). Meanwhile, *Slc45a2* KO resulted in significant decreases in TYR activity after 10 days of culture (Figure 1g). Pheomelanin was measured by reductive hydrolysis assays with hydriodic acid, and *Slc45a2* deficiency reduced pheomelanin abundance in the dorsal skin of mice aged 3 months (Figure 1h and Supplementary Figure S2a). Abundances of levodopa and its derivates 3-O-methyldopa were highly decreased in *Slc45a2*-KO cells (Supplementary Figure S2e), which indicated that the whole melanin biosynthesis pathway was blocked owing to low Tyr activity.

To identify the protein-protein interactions with SLC45A2, we transfected Flag-tagged SLC45A2 fusion protein (SLC45A2-Flag) into B16F10 cells (Supplementary Figure S2b and c). Mass spectrometry (MS) showed TYRP1 as a putative interacting protein with SLC45A2 (Supplementary Figure S2d). Coimmunoprecipitation from human embryonic kidney 293T cells confirmed direct protein-protein interaction between SLC45A2 and TYRP1 (Figure 1i). However, SLC45A2 was incapable of interacting with Tyr (Supplementary Figure S2f). Heterologous overexpression of SLC45A2-Flag pulled down endogenous TYRP1 in B16F10 cells (Figure 1j), and immunofluorescent staining showed a high level of colocalization between SLC45A2 and TYRP1 (Figure 1k). Knockdown of *Slc45a2* reduced the transcriptional level of *Tyrp1* and vice versa (Figure 1l and m). These experiments show that SLC45A2 is involved in melanogenesis by regulating TYR activity and physically interacting with TYRP1.

Deletion of H^+/glucose exporter SLC45A2 lowered the pH and induced glucose accumulation in melanosomes

Melanosome pH regulates TYR activity during melanogenesis (Ancans et al., 2001; Bellono et al., 2014). We measured melanosomal pH using Lysosensor Green DND-189, which specifically colocalized with the melanosome marker (Tyr-mCherry) (Supplementary Figure S3f and g). The mean fluorescence intensity of the lysosensor in KO was 10.3-fold stronger than in the WT (Figure 2a and Supplementary Figure S3a). A genetically encoded melanosome-localized pH sensor was expressed, and its fluorescent intensity is proportional to the melanosomal pH value (Ambrosio et al., 2016). *Slc45a2* KO had obviously reduced the mean fluorescence intensity of the melanosome-localized pH sensor compared with that in the WT, also supporting that KO has a lower melanosomal pH (Figure 2b and Supplementary Figure S3b). Treatment with 15 nM vacuolar-type ATPase inhibitor bafilomycin A1 can partially induce melanization and increase the number of stage III/IV mature melanosomes in KO (Figure 2c-e). These results showed that SLC45A2 regulates melanosomal pH and proton export from melanosomes.

We next explored the sugar transport activity of SLC45A2 by measuring the radioactive uptake of [14C(U)]-sucrose and 2-[1,2-3H(N)]-deoxy-D-glucose from isolated melanosomes. Uptake of [14C(U)]-sucrose and 2-[1,2-3H(N)]-deoxy-D-

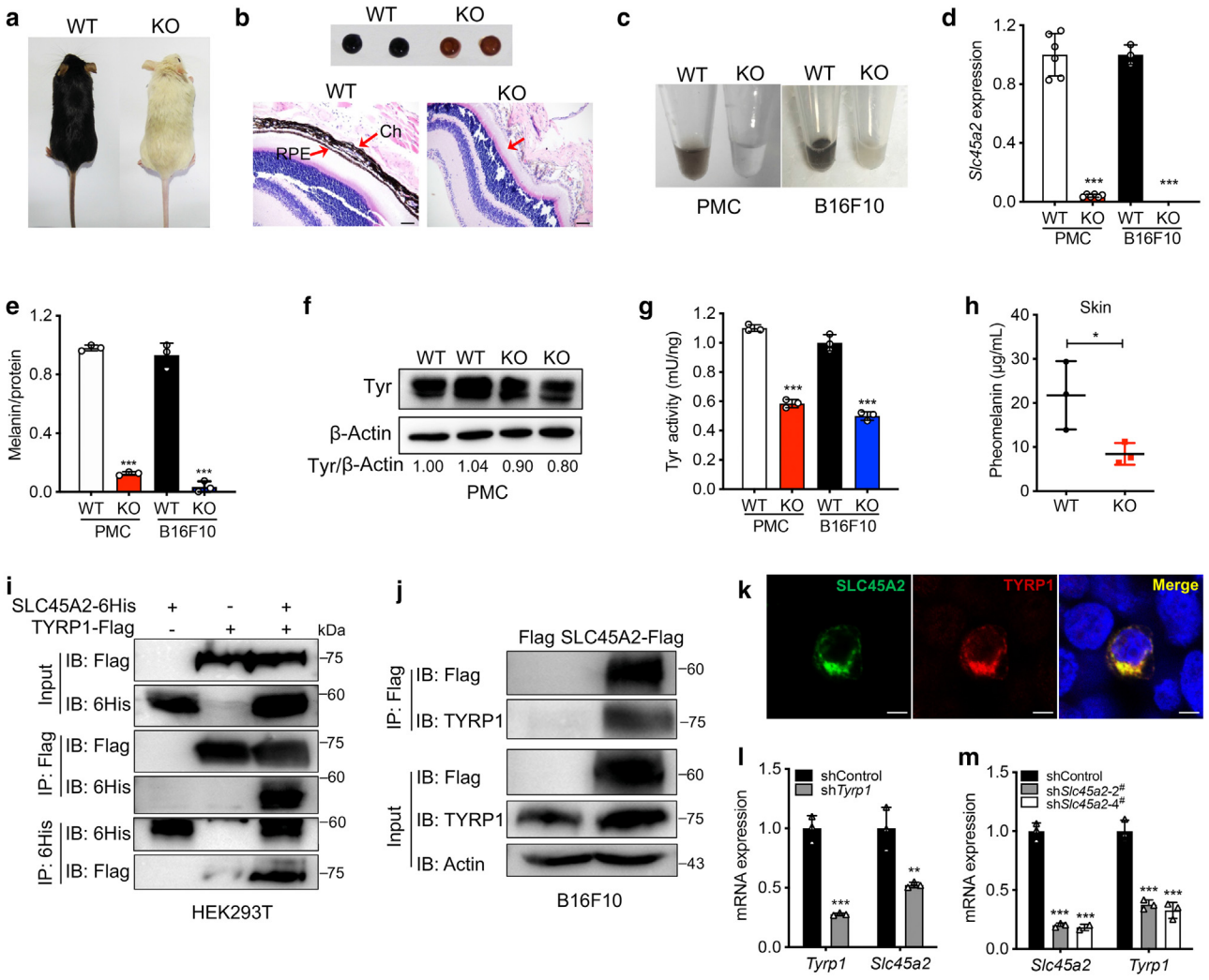

Figure 1. SLC45A2 regulates pigmentation by modulating Tyr activity and interacting with TYRP1. **(a)** Image of C57BL/6J a WT mouse (left) and a *Slc45a2*-KO mouse (right). **(b)** Images of mouse eyes and H&E staining of vertical sections prepared from the eyes; the red arrows indicate the RPE and the Ch. Bar = 40 μm. **(c)** KO of *Slc45a2* from PMCs and B16F10 melanoma cells resulted in clearly reduced pigment accumulation. **(d)** qPCR analysis of *Slc45a2* in WT and KO PMCs (n = 3). **(e)** Quantification of melanin content in WT and *Slc45a2*-KO PMCs and B16F10 cells (n = 3). **(f)** Western blotting against the TYR protein in WT and *Slc45a2*-KO PMCs sampled 6 and 10 days of culture. Data represent similar results from three replicate blots. **(g)** TYR activity assays using total protein extracts from WT and *Slc45a2*-KO PMCs and B16F10 cells (n = 3). **(h)** Pheomelanin content in dorsal skin from WT and *Slc45a2*-KO mice aged 3 months, measured by HPLC, with 4-AHP standards (n = 3). **(i)** co-IP of overexpressed SLC45A2-6His and TYRP1-Flag fusion proteins in HEK293T cells. A total of 5% of the cell lysate was used as the input. Data are representative of three experiments. **(j)** Detection of SLC45A2 interactions with endogenous TYRP1 by immunoprecipitation expressed in B16F10 cells (repeated three times). **(k)** Immunofluorescence localization of SLC45A2 and TYRP1 in HEK293T cells coexpressing both SLC45A2 and TYRP1 (repeated three times). The merged image shows the extent of colocalization. Bar = 5 μm. **(l)** Knockdown of *Tyrp1* in B16F10 cells; mRNA expression levels of *Tyrp1* and *Slc45a2* were detected by qPCR (n = 3). **(m)** Knockdown of *Slc45a2* in B16F10 cells; mRNA expression levels of *Tyrp1* and *Slc45a2* were detected by qPCR (n = 3). For **d**, **e**, **g**, **h**, **l**, and **m**, data are shown as mean ± SD; Student's *t*-tests were used for the indicated comparisons. $^*P < 0.05$, $^{**}P < 0.01$, and $^{***}P < 0.001$. 4-AHP, 4-amino-3-hydroxyphenylalanine; 6His, six histidine tag; Ch, choroid; co-IP, coimmunoprecipitation; HEK293T, human embryonic kidney 293T; HPLC, high-performance liquid chromatography; IB, immunoblotting; IP, immunoprecipitation; KO, knockout; PMC, primary melanocyte; RPE, retinal pigment epithelium; shControl, control short-hairpin RNA; sh*Slc45a2*, short-hairpin RNA targeting *Slc45a2*; sh*Typ1*, short-hairpin RNA targeting *Typ1*; TYR, tyrosinase; WT, wild type.

glucose was increased by ~2.5-fold and ~1.9-fold, respectively, 15 minutes after treatment in KO melanosomes compared with that in WT ones (Figure 2f). In addition, glucose uptake signal of 2-deoxy-2-[(7-nitro-2,1,3-benzoxadiazol-4-yl) amino]-D-glucose was relatively weak and uniformly distributed in the cytoplasm of WT cells, whereas it showed a punctate and stronger melanosomal accumulation in *Slc45a2*-KO cells. Colocalization analyses in KO cells showed about twice higher Pearson's correlation coefficient than in WT cells (Figure 2g) (0.42 for WT cells, 0.81 for KO cells). Collectively, *Slc45a2* deficiency led to the accumulation of glucose within melanosomes, indicating that SLC45A2 functions as the glucose/H^+ exporter of melanosomes into the cytosol.

We next modeled a predicted three-dimensional structure of both mouse and human SLC45A2 using Robetta and carried out a docking of various sugar molecules to both models (Supplementary Figure S3c). The predicted binding pocket for D-glucose in mouse SLC45A2 along with interacting residues is illustrated in Figure 2h. In addition, we compared the

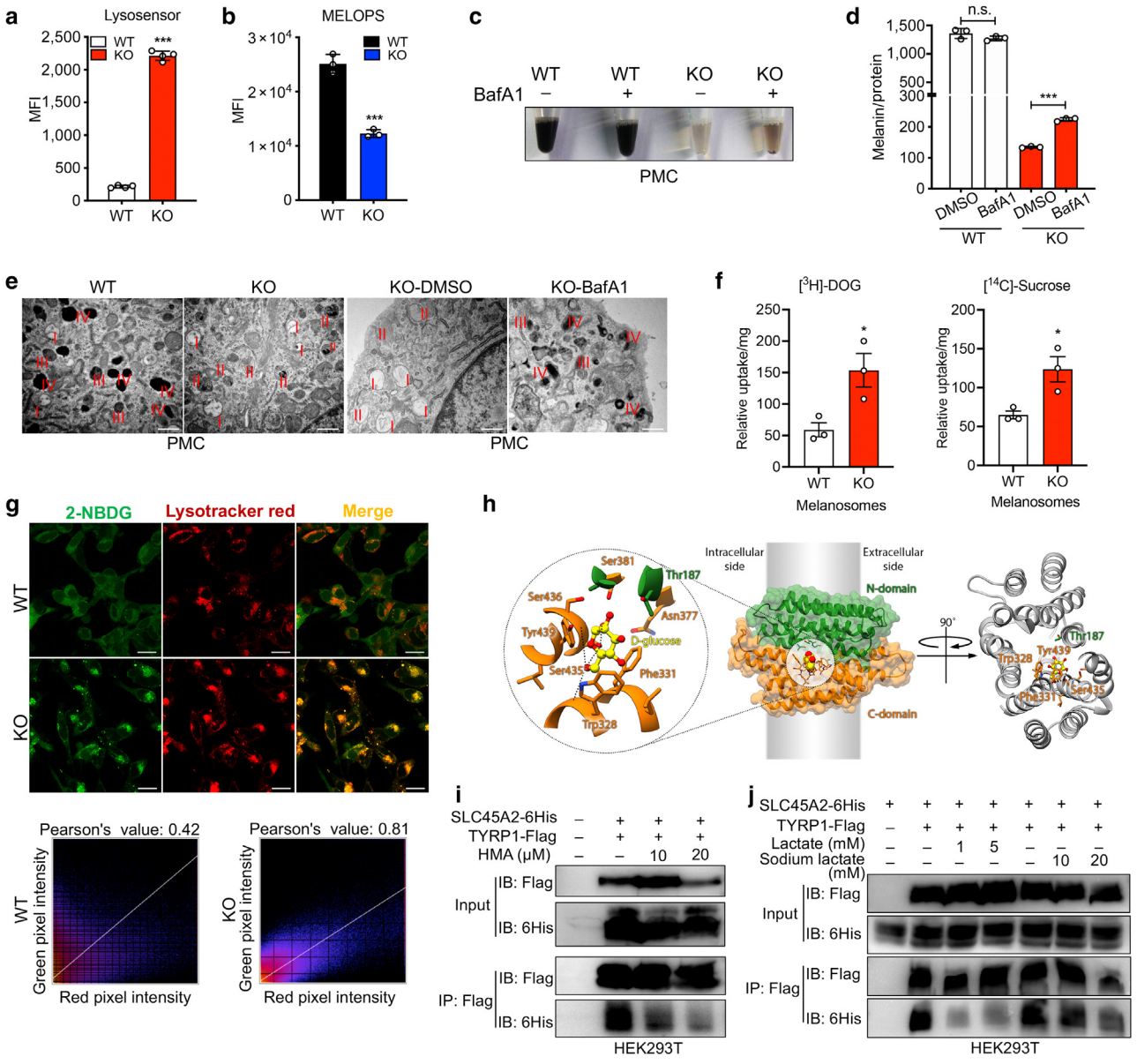

Figure 2. SLC45A2 exports protons and glucose from the melanosome into the cytosol. **(a)** MFI of WT and *Slc45a2*-KO melanocytes stained with the lysosensor DND-189 pH indicator (1 μM, 37 °C prewarmed) for 40 min (n = 4). **(b)** MFI of WT and *Slc45a2*-KO B16F10 cells expressing the MELOPS plasmid (n = 3). **(c)** Rescue of melanocyte melanization by treatment with the V-ATPase inhibitor BafA1 (15 nM, 9 hours). **(d)** Melanin content of PMCs treated with 15 nM BafA1 for 9 hours (n = 3). **(e)** TEM images of *Slc45a2*-KO PMCs treated with BafA1 (or DMSO control) at ×50,000 magnification; the red roman numerals represent different stages of melanosomes (premature melanosomes: stages I and II, mature melanosomes: stages III and IV). Bar = 500 nm. **(f)** Uptake of the radioactive ^{14}C-sucrose and glucose analog ^{3}H-DOG of isolated melanosomes from WT and *Slc45a2*-KO B16F10 cells (n = 3). **(g)** Colocalization of lysotracker (red) and a fluorescent glucose analog (2-NBDG) in WT and *Slc45a2*-KO B16F10 cells. Pearson's correlation of lysotracker (red) and 2-NBDG (green) signal intensity (pixel) is shown below. Bar = 20 μm. **(h)** Homology-based 3D structural model of mouse SLC45A2 based on *E. coli* proton/xylose symporter XylE [PDB ID: 4GBY] as the template, shown in ribbon representation. Analysis of residue conservation carried out using ConSurf (Ashkenazy et al., 2016) further revealed that the binding pocket containing polar residues such as Thr187, Asn377, Ser381, Ser435, and Ser436 could form favorable hydrogen bonds with the oxygen atoms of glucose and other similar sugar molecules. **(i)** Immunoprecipitation with SLC45A2-6His and TYRP1-Flag, performed in HEK293T cells treated with 0, 10, or 20 μM HMA, an inhibitor of the NHE, for 24 hours. **(j)** Immunoprecipitation with SLC45A2-6His and TYRP1-Flag, performed in HEK293T cells treated with 1 mM L-lactate, 5 mM L-lactate, 10 mM sodium lactate, or 20 mM sodium lactate for 24 hours. For **a**, **b**, and **d**, data are shown as mean ± SEM; Student's *t*-tests were used for the indicated comparisons. $*P < 0.05$, $**P < 0.01$, and $***P < 0.001$. ^{14}C-sucrose, [14C(U)]-sucrose; 2-NBDG, 2-deoxy-2-[(7-nitro-2,1,3-benzoxadiazol-4-yl) amino]-D-glucose; 3D, three-dimensional; ^{3}H-DOG, 2-[1,2-3H(N)]-deoxy-D-glucose; 6His, six histidine tag; BafA1, bafilomycin A1; HEK293T, human embryonic kidney 293T; HMA, 5-N, N-hexamethylene amiloride; IB, immunoblotting; IP, immunoprecipitation; KO, knockout; MELOPS, melanosome-localized pH sensor; min, minute; MFI, mean fluorescence intensity; NHE, sodium ion/proton exchanger; n.s., not significant; PMC, primary melanocyte; TEM, transmission electron microscopy; V-ATPase, vacuolar-type ATPase; WT, wild type.

structure predicted by Robetta with the one predicted by AlphaFold (Jumper et al., 2021) and found that both predicted structures largely agreed with respect to the 12-transmembrane helices and the organization of the binding pocket (Supplementary Figure S3d).

SLC45A2 localizes to lysosomes when ectopically expressed in nonmelanocytic cells (Le et al., 2020). Immunoprecipitation results showed that sodium ion/H^+ exchanger inhibitor 5-N, N-hexamethylene amiloride decreased lysosomal pH to weaken the interaction between SLC45A2 and TYRP1 in a dose-dependent manner (Figure 2i and Supplementary Figure S2g and h). In addition, this interaction was also impaired when treated with 1 or 5 mM lactate, whereas the addition of sodium lactate had no effect (Figure 2j). These results suggested that the pH also influences the interaction between SLC45A2 and TYRP1.

Deficiency of *Slc45a2* significantly upregulated glycolytic enzymes and enhanced glycolysis

RNA-sequencing transcriptomics analysis (Supplementary Table S1) showed significantly higher mRNA expression levels of glycolytic enzymes in *Slc45a2*-KO than in WT cells (Figure 3a and b). Consistently, the protein levels of SLC2A1, HK1, and LDHA in glycolytic pathway were clearly increased, whereas phosphorylated AMPKα (Thr172) was suppressed after *Slc45a2* deletion (Figure 3c). *Slc2a1* and *Slc2a8* had higher expression levels than others, which might be the predominant transporters for glucose uptake in melanocytes (Supplementary Figure S4a). We applied liquid chromatography-MS-based glycolytic flux with U-$^{13}C_6$ glucose-treated melanocytes to measure the glycolytic metabolites (Supplementary Table S2). Larger fractions of ^{13}C-labeled pyruvate and ^{13}C-labeled lactate in the m+3 isotopomer forms were detected in KO cells than in WT cells for both PMCs and B16F10 cells (Figure 3d and e). Moreover, lactate excretion of KO cells is significantly higher than that of WT cells when m+3 lactate levels from the culture media were detected using liquid chromatography-MS (Figure 3f). Global chromatin accessibility status was analyzed using the assay for transposase-accessible chromatin using sequencing (Supplementary Figure S3e). Accordingly, *Slc45a2* deficiency increased the accessibility to the promoter regions of *Slc2a1*, *Hk1*, and *Pgam1* (Figure 3g-i), showing a more active status of these glycolysis gene transcriptions.

Metabolomic analysis of Flp-In human embryonic kidney 293 cells (human embryonic kidney 293F) stably overexpressing mouse *Slc45a2* (*Slc45a2*), human *SLC45A2* (*SLC45A2*) cells, or empty vector-transfected control (Supplementary Figure S4b and Supplementary Table S3) showed that multiple metabolites of glycolysis such as glucose/fructose/mannose-6-phosphate, fructose 1,6-bisphosphate, pyruvic acid, and L-lactic acid were significantly reduced in both *Slc45a2*- and *SLC45A2*-overexpressed human embryonic kidney 293F cells (Figure 3j and Supplementary S4c). Gene Expression Omnibus expression data (GSE21565) showed that glycolytic genes were significantly elevated in the light human melanocytes harboring the 374F allele of *SLC45A2* gene compared with those in the dark ones (Supplementary Figure S4d). Collectively, these results show that *Slc45a2* deficiency enhances glycolysis in the melanocytes.

Melanosome is an active glucose-metabolizing organelle during a loss of *Slc45a2*

Intriguingly, many glycolytic proteins were detected with liquid chromatography-tandem MS-based proteomics in the purified melanosomes (Supplementary Table S4 and Supplementary Figure S4e). The abundance of HK1, PKM2, LDHA, and other glycolytic proteins was significantly higher in *Slc45a2*-KO melanosomes than in WT ones (Figure 4a). We next characterized the protein abundances from whole-cell lysates, mitochondria, the cytosolic fraction, and purified melanosome components. HK1, PKM2, and LDHA had much higher levels in isolated melanosomes after *Slc45a2* deletion (Figure 4b), which indicates that glycolytic enzymes potentially perform glycolysis in melanosomes independent of cytosol. Therefore, we incubated ^{13}C-labeled glucose (i.e., [U-$^{13}C_6$] glucose) with WT and *Slc45a2*-KO cells and isolated melanosomes. KO melanosomes contained more ^{13}C-labeled pyruvate and ^{13}C-labeled lactate in the m+3 isotopomer forms than WT melanosomes (Figure 4c and Supplementary Table S5). Moreover, we isolated melanosomes firstly, followed by [U-$^{13}C_6$] glucose labeling, and found that glycolytic intermediate m+6 isotopomer of G6P, m+3 isotopomer of DHAP, and lactate products remained produced significantly higher in KO melanosomes than in WT melanosomes (Figure 4d and Supplementary Table S5).

Next, we measured the enzymatic activities of glycolytic enzymes. HK, PKM, and LDHA activities were about 2.8-, 3.0-, and 2.0-fold higher in KO melanosomes than in WT melanosomes, respectively (Figure 4e). Immunofluorescent staining of HK1 and LDHA with late melanosomal marker TYRP1 also revealed a high level of colocalization extent in KO cells, which is represented by Pearson's correlation (Figure 4f and Supplementary Figure S4f-h). In summary, these data showed that melanosomes might be a glycosome-like organelle and that *Slc45a2* deficiency enhanced glycolysis activity in melanosomes.

Enhanced glycolysis attenuated melanogenesis by acidifying melanosomal pH in *Slc45a2*-KO cells

Pyruvate and lactate are products of anaerobic glycolysis that contribute to cell acidification (Ganapathy et al., 2009). *Slc45a2* deficiency increased glucose consumption and lactate excretion in both PMC and B16F10 cells under high glucose (HG) (4.5 g/l) or low glucose (LG) (1.0 g/l) media (Figure 5a and b). Glycolysis and glycolytic capacity were significantly increased under HG and LG media in KO compared with those in WT when measured by the extracellular acidification rate (Figure 5c and d). As expected, the mean fluorescence intensity of lysosensor significantly weakened under LG media compared with that under HG condition in KO cells (Figure 5e and Supplementary S5a), and the addition of glycolytic inhibitor 2-deoxy-D-glucose could also increase melanogenesis by alkalinizing melanosomal pH as effectively as LG media (Figure 5f and Supplementary S5b).

Short-hairpin RNA-mediated knockdown of *Slc2a1* and *Ldha* was used in both WT and KO B16F10 cells

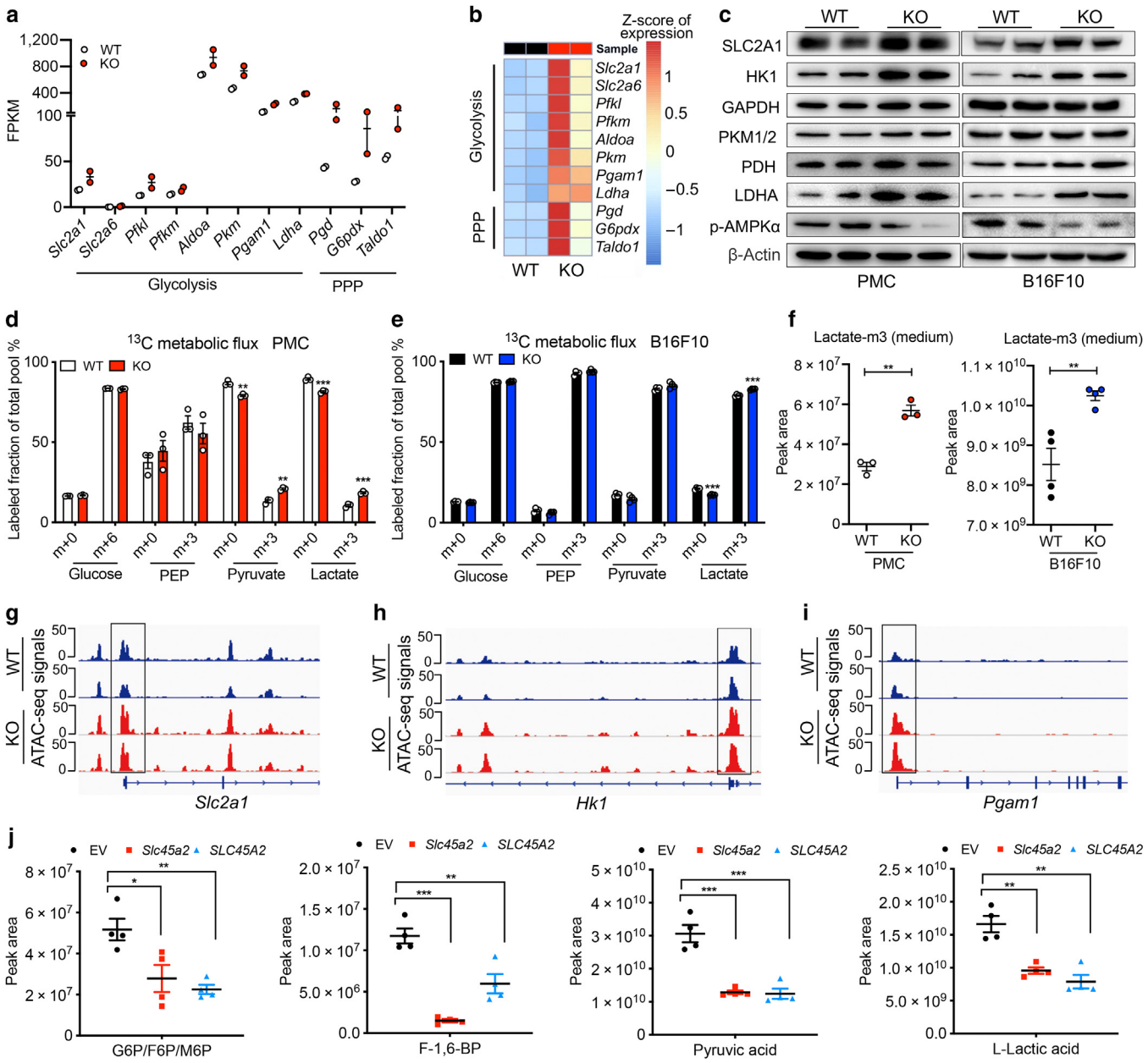

Figure 3. Characterization of SLC45A2 in the regulation of glycolytic states. **(a)** Mean FPKM from RNA-seq data of glycolysis and PPP genes in WT and *Slc45a2*-KO primary melanocytes in duplicates. **(b)** Heatmap of RNA-seq data showing the expression levels of genes encoding enzymes for glycolysis and PPP in WT and *Slc45a2*-KO PMCs. **(c)** Western blotting of glycolytic proteins in WT and *Slc45a2*-KO PMCs and B16F10 cells. **(d, e)** LC–MS–based analysis of [U-$^{13}C_6$] glucose in WT and *Slc45a2*-KO PMCs (n = 3) and B16F10 cells (n = 4); shown is the percentage of isotopically labeled molecules of the indicated metabolites (m represents the number of isotopes per molecule). **(f)** Measurement of m+3 isotopomer lactate excretion in cell culture medium collected from PMC (n = 3) and B16F10 (n = 4) cells. **(g–i)** The ATAC-seq signals of glucose metabolism genes, including *Slc2a1*, *Hk1*, and *Pgm1*. The rectangles indicate promoter regions. **(j)** LC–MS–based untargeted metabolomics analysis showing that four glycolytic intermediates—G6P/F6P/M6P, F-1,6-BP, pyruvic acid, and L-lactic acid—were significantly decreased in HEK293 SLC45A2 cells compared with those in the control group (n = 4). For **d**, **e**, **f**, and **j**, data are shown as the mean ± SEM. Student's *t*-tests were used for the indicated comparisons. $^*P < 0.05$, $^{**}P < 0.01$, and $^{***}P < 0.001$. ATAC-seq, assay for transposase-accessible chromatin using sequencing; F-1,6-BP, fructose 1,6-bisphosphate; FPKM, fragments per kilobase per million mapped reads; G6P/F6P/M6P, glucose/fructose/mannose-6-phosphate; HEK293, human embryonic kidney 293; HK1, Hexokinase 1; KO, knockout; LC–MS, liquid chromatography–mass spectrometry; LDHA, lactate dehydrogenase A; p-AMPKα, phosphorylated AMPKα; PDH, pyruvate dehydrogenase; PEP, phosphoenolpyruvate; PKM, pyruvate kinase; PMC, primary melanocyte; PPP, pentose phosphate pathway; RNA-seq, RNA-sequencing; WT, wild type.

(Supplementary Figure S5c and d). Short-hairpin RNA targeting *Slc2a1* and short-hairpin RNA targeting *Ldha* significantly increased melanogenesis in KO cells, suggesting that the glycolysis pathway plays an inhibitory role during melanogenesis (Supplementary Figure S5e and f). We treated WT PMCs with mitochondrial pyruvate transporter inhibitor UK5099, which can block oxidative phosphorylation and elevate lactate levels (Davies et al., 2017). UK5099 (50 μM, 48 hours) decreased melanogenesis and TYR activity in WT cells (Figure 5g and Supplementary Figure S5g). LDHA-

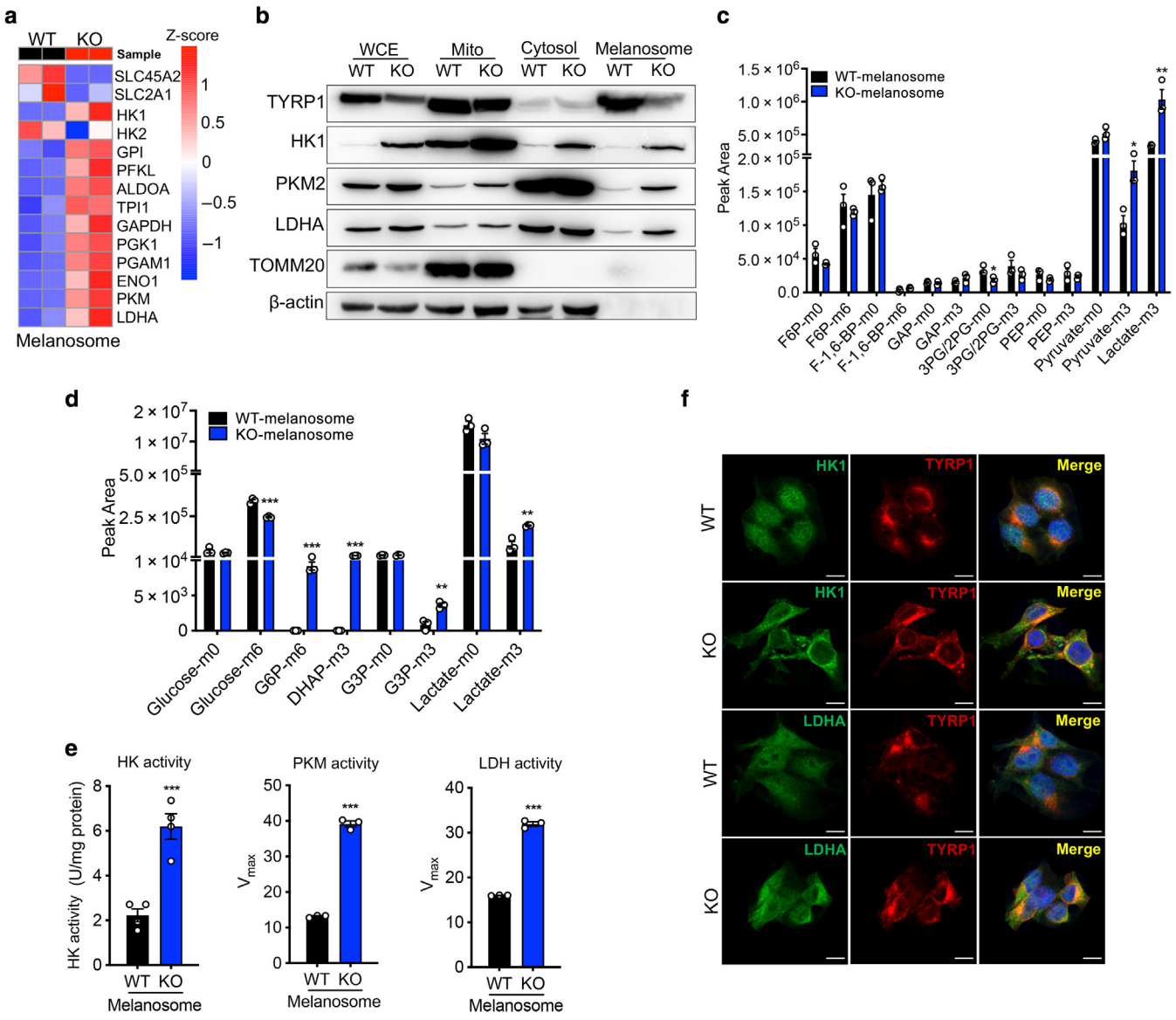

Figure 4. Melanosomes are active glucose-metabolizing organelles. **(a)** Heatmap of LC-MS/MS–based proteomics showing the SLC45A2 and glycolytic protein abundances represented by peak areas in isolated WT and KO melanosomes in duplicates. **(b)** Immunoblotting of extracted glycolytic proteins from subcellular compartments. Examined samples included WCE, Mito, the cytosol, and melanosomes of WT and *Slc45a2*-KO B16F10 cells. TYRP1 was the protein marker for melanosomes, TOMM20 was the marker for mitochondria, and β-actin was the marker for both WCE and the cytosol. **(c)** WT and *Slc45a2*-KO B16F10 cells were first labeled with [U-$^{13}C_6$] glucose in culture medium at 37 °C for 6 hours, then melanosomes were isolated and subjected to an 80% methanol extraction. The extracts were then measured by LC–MS–based ^{13}C-labeled metabolic flux analysis (F6P, F-1,6-BP, GAP, 3PG/2PG, PEP) (n = 3). **(d)** WT and *Slc45a2*-KO melanosomes were first isolated and then labeled with [U-$^{13}C_6$] glucose at 37 °C for 1 hour. Metabolites were extracted by 80% methanol and measured by LC–MS–based ^{13}C-labeled metabolic flux analysis (G6P, DHAP, G3P) (n = 3). **(e)** Enzymatic activities of HK (n = 4), PKM (n = 3), and LDH (n = 3) were measured in extracts from WT and *Slc45a2*-KO melanosomes. **(f)** Confocal immunofluorescence microscopy of B16F10 cells immunolabeled with antibodies against HK1 (or LDHA) (green) or TYRP1 (red); nuclei were stained with DAPI (blue). Bar = 10 μm. For **c**, **d**, and **e**, data are shown as mean ± SEM. Student's *t*-tests were used for the indicated comparisons. *$P < 0.05$, **$P < 0.01$, and ***$P < 0.001$. 3PG/2PG, 3-phosphoglycerate/2-phosphoglycerate; DHAP, dihydroxyacetone phosphate; F-1,6-BP, fructose 1,6-bisphosphate; F6P, fructose-6-phosphate; G6P, glucose-6-phosphate; GAP, glyceraldehyde 3-phosphate; HK, hexokinase; KO, knockout; LC–MS, liquid chromatography–mass spectrometry; LC-MS/MS, liquid chromatography with tandem mass spectrometry; LDH, lactate dehydrogenase; Mito, mitochondria; PEP, phosphoenolpyruvate; PKM, pyruvate kinase; WCE, whole-cell lysate; WT, wild type.

specific inhibitor, GSK2837808A (10 μM, 48 hours), was utilized on KO PMCs, showing that melanin production and TYR activity were significantly elevated after treatment (Figure 5h and Supplementary S5h). Overall, these results showed that pharmacologically or genetically inhibition of glycolysis could promote melanogenesis by alkalinizing melanosomal pH.

Slc45a2 deficiency promoted melanoma cell survival during glucose starvation

Next, we investigated whether *Slc45a2* deficiency would trigger differential cellular responses to glucose starvation. We exposed WT and *Slc45a2*-KO cells to HG, LG, or glucose-free (0 g/l) media for 48 hours and measured cell viability and apoptosis (Figure 5i). There were no significant

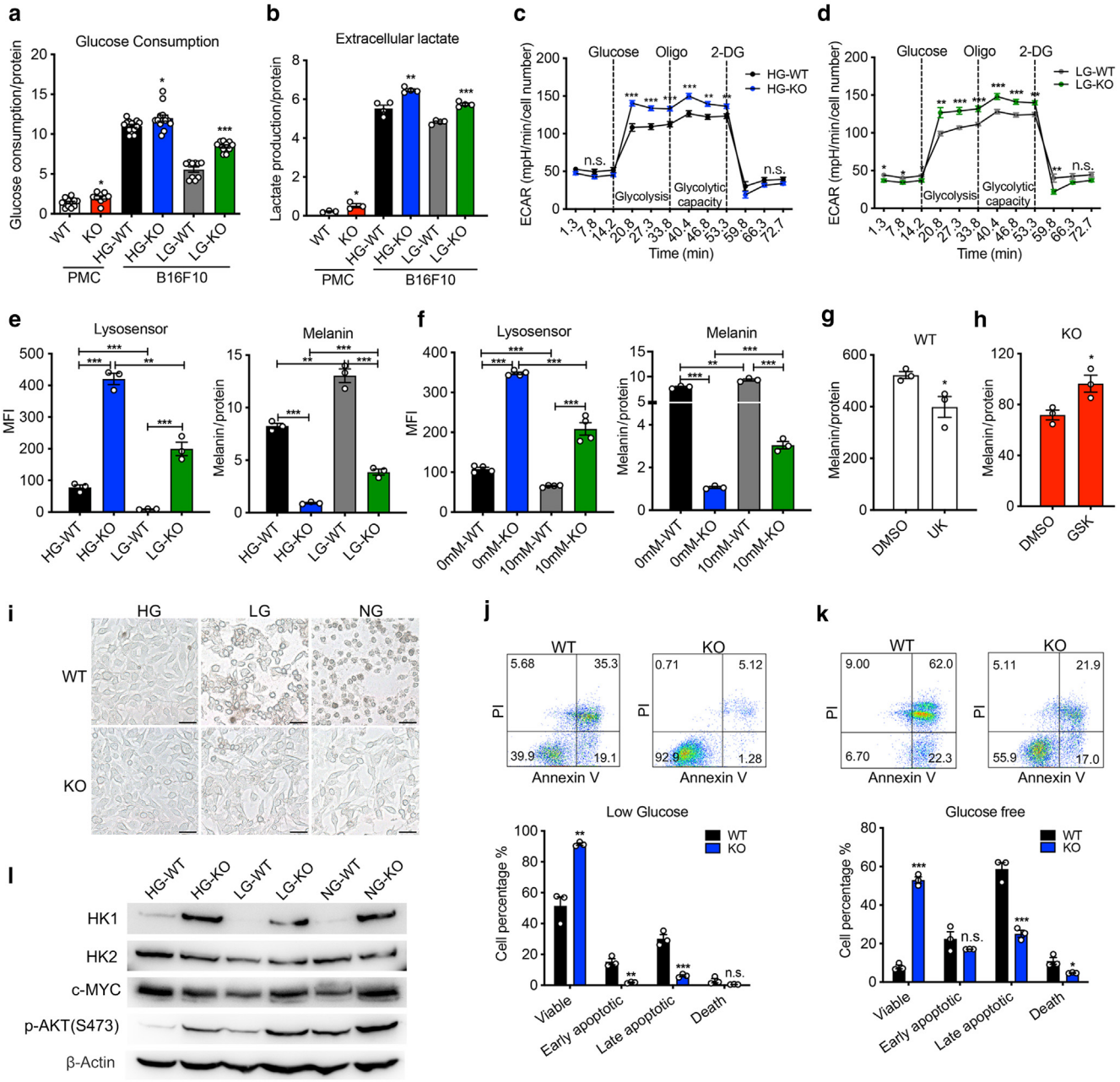

Figure 5. *Slc45a2* KO promotes cell survival during glucose starvation and attenuates pigmentation by enhanced glycolysis. **(a)** Glucose consumption was examined (using a glucose assay kit) in PMC (n = 10) and in B16F10 cells cultured in HG (4.5 g/l, n = 14) or LG (1.0 g/l, n = 10) media for 24 hours. **(b)** Lactate excretion was examined using an L-lactate assay kit in PMCs (n = 3) and in B16F10 cells cultured in HG (n = 4) or LG (n = 4) media for 24 hours. **(c, d)** ECAR was examined using Seahorse XFe96 analyzer under HG or LG media for 24 hours. Relative glycolysis levels and glycolytic capacity are normalized to cell numbers (n = 10). **(e)** Measurement of melanosomal pH and melanin content of WT and *Slc45a2*-KO B16F10 cells cultured in HG or LG media for 24 hours (n=3). **(f)** Measurement of melanosomal pH and melanin content of WT and *Slc45a2*-KO B16F10 cells treated with 10 mM glycolysis inhibitor 2-DG for 12 hours (n = 3). **(g)** Melanin content in WT PMCs treated with DMSO or the mitochondrial pyruvate transporter inhibitor UK5099 (50 μM) for 48 hours (n = 3). **(h)** Melanin content in *Slc45a2*-KO primary melanocytes treated with DMSO or the LDHA-specific inhibitor GSK2837808A (10 μM) for 48 hours (n = 3). **(i)** Bright-field cellular morphology of WT and *Slc45a2*-KO B16F10 cells cultured in HG, LG, or NG (0 g/l) media for 48 hours. Bar = 50 μm. **(j, k)** Annexin V-FITC/PI staining was used to determine the percentage of apoptotic cells in WT and *Slc45a2*-KO B16F10 cells after 48 hours of culture in LG and NG media (n = 3). Annexin V and PI negative indicate viable cells, Annexin V positive and PI negative indicate early apoptosis, Annexin V and PI positive indicate late apoptosis, and Annexin V negative and PI positive indicate death. **(l)** Western blotting showing the protein level of HK1, HK2, c-MYC, p-AKT (S473), cleaved caspase 9, and cleaved caspase 3 in WT and KO cells cultured in HG, LG, or NG media. For **a–d**, **g, h**, **j, and k**, Student's *t*-tests were used for the indicated comparisons. Two-way ANOVA followed by Tukey's multiple comparison test was used for **e** and **f**. $*P < 0.05$, $**P < 0.01$, and $***P < 0.001$). 2-DG, 2-deoxy-D-glucose; ECAR, extracellular acidification rate; GSK, GSK2837808A; HG, high glucose; HK, hexokinase; KO, knockout; LDHA, lactate dehydrogenase A; LG, low glucose; MFI, mean fluorescence intensity; min, minute; NG, glucose-free; n.s., not significant; p-AKT, phosphorylated protein kinase B; PI, propidium iodide; PMC, primary melanocyte; UK, UK5099; WT, wild type.

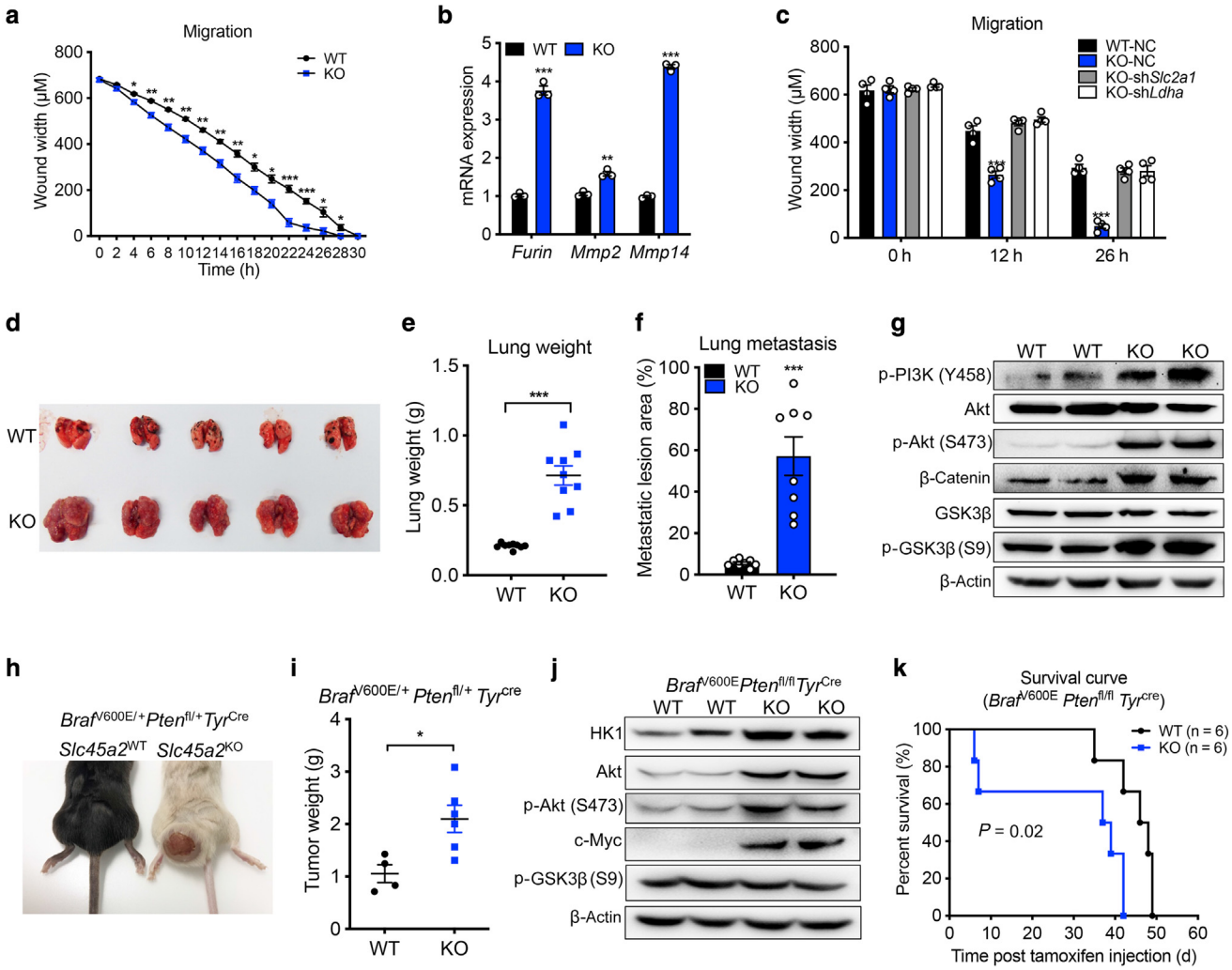

Figure 6. *Slc45a2* deficiency accelerates melanoma metastasis in both cell model and *Braf/Pten/Tyr*^{Cre} melanoma model. **(a)** Analysis of cell migration in a time-lapse wound healing assay; the wound width was used to represent the migration capacity of cells (n = 3). **(b)** mRNA expression of *Furin*, *Mmp2*, and *Mmp14*, assessed by qPCR (n = 3). **(c)** Analysis of cell migration in a time-lapse wound healing assay; the wound width was measured in WT control (WT NC), *Slc45a2*-KO control (KO NC), *Slc45a2* KO with *Slc2a1* knockdown (KO sh*Slc2a1*), and *Slc45a2* KO with *Ldha* knockdown (KO sh*Ldha*) at 0, 12, or 26 hours (n = 4 samples per group, with the experiments repeated three times). **(d)** Images of mouse lungs 14 days after tail vein injection of 300,000 WT or *Slc45a2*-KO B16F10 cells in nude mice. **(e, f)** Lung weight (n = 9) and percentage of lung area covered by metastatic tumor areas (n = 8). **(g)** The protein abundance of PI3K–Akt signaling pathway components in WT and *Slc45a2*-KO B16F10 cells, analyzed by western blotting. **(h)** Representative images of *Braf*$^{V600E/+}$*Pten*$^{fl/+}$*Tyr*^{Cre}*Slc45a2*^{WT} and *Braf*$^{V600E/+}$*Pten*$^{fl/fl}$*Tyr*^{Cre}*Slc45a2*^{KO} mice. Adult mice aged 4 weeks were shaved and treated topically with 10 μl of 1.55 mg/ml of 4-OHT for 3 consecutive days. Application of 4-OHT onto the skin of these mice activates Tyr^{Cre} selectively in melanocytes, inducing the expression of oncogenic *Braf*^{V600E} and knocking out the *Pten* gene. **(i)** Tumor weights for *Braf*$^{V600E/+}$*Pten*$^{fl/fl}$*Tyr*^{Cre} *Slc45a2*^{WT} (n = 4) and *Braf*$^{V600E/+}$*Pten*$^{fl/fl}$*Tyr*^{Cre} *Slc45a2*^{KO} (n = 6) mice. **(j)** The protein abundance of HK1, c-MYC, and PI3K–AKT signaling pathway components in dorsal tumor tissue isolated from WT or *Slc45a2*-KO genotypes under the genetic background of *Braf*^{V600E} *Pten*$^{fl/fl}$ *Tyr*^{cre}, analyzed by western blotting. **(k)** Kaplan–Meier survival curve of mice with the indicated WT (n = 6) and *Slc45a2*-KO (n = 6) genotypes under the genetic background of *Braf*^{V600E} *Pten*$^{fl/fl}$ *Tyr*^{cre}, following intraperitoneal administration of 150 μl 10 mg/ml tamoxifen suspension in corn oil on 3 consecutive days. Log-rank (Mantel–Cox) test of survival plots, indicating a statistically significant difference between the WT and KO genotypes ($P = 0.02$) was performed. For **a–c**, **e**, **f**, and **i**, data are shown as mean ± SEM; Student's *t*-tests were used for the indicated comparisons. *$P < 0.05$, **$P < 0.01$, and ***$P < 0.001$. 4-OHT, 4-hydroxytamoxifen; AKT, protein kinase B; d, day; h, hour; KO, knockout; MMP, matrix metalloproteinase; NC, nontargeting control; p-AKT, phosphorylated protein kinase B; p-PI3K, phosphorylated phosphatidylinositol 3-kinase; PI3K, phosphatidylinositol 3-kinase; sh*Ldha*, short-hairpin RNA targeting *Ldha*; sh*Slc2a1*, short-hairpin RNA targeting *Slc2a1*; WT, wild type.

differences in viable and apoptotic cells between WT and KO under HG media, but the viable cell numbers in KO were significantly higher under LG and glucose-free media (Figure 5j and k). HK1 and phosphorylated protein kinase B (AKT) (S473) were increased in KO under all the three conditions, whereas c-MYC was higher in KO than in WT under LG and glucose-free conditions (Figure 5l). These results collectively indicate that *Slc45a2*-deficient cells are more resistant to glucose starvation-induced apoptosis than WT cells.

Slc45a2 deficiency accelerates melanoma metastasis and progression by activating phosphatidylinositol 3-kinase/Akt signaling pathway

On the basis of elevated glycolysis and increased resistance to glucose starvation in KO cells, we characterized the role of

SLC45A2 in melanoma progression. Wound healing assay indicated a significant reduction in cell-free gaps with *Slc45a2* deficiency (Supplementary Figure S6a and Figure 6a). mRNA expression of *Furin* and matrix metalloproteinase (MMP) genes *Mmp2* and *Mmp14*, which facilitate cancer migration and invasion, were significantly increased in KO cells (Figure 6b). *Slc45a2* KO with short-hairpin RNA targeting *Slc2a1* or short-hairpin RNA targeting *Ldha* displayed attenuated cell migration compared with vehicle control (Figure 6c). Taken together, these results indicated that *Slc45a2* deficiency promoted melanoma metastasis in vitro.

We next investigated the effect of SLC45A2 on tumor growth and distant metastasis in vivo. *Slc45a2* deficiency did not alter melanoma growth (Supplementary Figure S6b and c) but largely promoted lung metastasis by measuring lung weight (Figure 6d and e) and lung metastatic lesion area (Figure 6f). Phosphatidylinositol 3-kinase (PI3K)/AKT pathway is frequently activated in melanoma and is proposed as an attractive drug target to improve clinical outcomes (Kwong and Davies, 2013). KO cells showed markedly increased phosphorylation of PI3K (phosphorylated PI3K, Tyr458), phosphorylated AKT (Ser473), glycogen synthase kinase 3β, phosphorylated glycogen synthase kinase 3β (Ser9), and β-catenin expression (Figure 6g), showing that AKT signaling is remarkably elevated to accelerate melanoma metastasis in *Slc45a2* deficiency.

Slc45a2-KO mice were crossed with the melanoma mice harboring $Braf^{V600E}/Pten^{flox}/Tyr^{Cre}$ transgene (Dankort et al., 2009) to study metastasis in melanoma mice model. *Slc45a2* deficiency in $Braf^{V600E/+}Pten^{fl/fl}Tyr^{Cre}$ mice resulted in faster and more aggressive growing melanoma than in WT (Figure 6h and i). Histological analysis of melanoma sections revealed increased tumor number (Supplementary Figure S6d) and marked splenomegaly in $Braf^{V600E/+}Pten^{fl/fl}Tyr^{Cre}$ *Slc45a2*-KO mice (Supplementary Figure S6e). HK1, AKT, phosphorylated AKT (S473), and c-MYC were also increased in KO abdominal skin tumors from $Braf^{V600E}Pten^{fl/fl}Tyr^{Cre}$ metastatic melanoma mice (Figure 6j). Overall survival was shortened by *Slc45a2* deletion for the $Braf^{V600E}Pten^{fl/fl}Tyr^{Cre}$ mice (Figure 6k), and the skin specimen from KO mice had more metastatic sites (Supplementary Figure S6f). Collectively, these data suggest that *Slc45a2* KO accelerates melanoma metastasis and progression in vivo and in vitro by reprogramming glucose metabolism.

DISCUSSION

SLC45A2 is proposed as a putative sugar transporter, mainly transporting disaccharide sucrose (Reinders and Ward, 2015; Vitavska and Wieczorek, 2017). Hyperosmotic stress resulting from sucrose imbalance disrupts vesicle trafficking and inhibits mature melanosome formation (Meyer et al., 2011). However, no obvious morphological changes happened in *Slc45a2*-KO melanosomes, such as size, shrinking, or swelling caused by osmotic pressure alternation (Figure 2e). Meanwhile, when sucrose enters mammalian cells, it breaks down to fructose and glucose quickly, rarely in disaccharide form (Park et al., 2017b). We did not detect any free sucrose in our metabolomic data (Supplementary Tables S2 and S3), and melanocytic cells can still synthesize melanin in the medium without a sucrose supplement. Therefore, we concluded that SLC45A2 was an H^+-coupled glucose exporter in melanosomes.

Intriguingly, glycolytic enzymes and metabolites were detected in relatively high abundance in KO melanosomes (Supplementary Table S4), which raised the possibility that melanosomes may be an active glucose-metabolizing organelle. When isolated melanosomes were incubated with ^{13}C-labeled glucose, many labeled glycolytic metabolites were detected inside them, and enzymatic activities of HK1, PKM2, and LDHA were significantly increased from KO melanosomes (Figure 4c-e). Notably, peroxisomes of the protist trypanosomatid parasites seclude the majority of glycolytic enzymes and hence are called glycosomes (Haanstra et al., 2016). A previous study also reported that all essential glycolytic enzymes moonlight in the nucleus to perform the canonical and noncanonical functions (Boukouris et al., 2016). However, the functions of glycolysis that occurred in melanosomes need to be further investigated.

Deleting *Slc45a2* made melanoma cells more resistant to apoptosis and accelerated melanoma progression by upregulating PI3K/AKT pathway. PI3K/AKTt signaling has diverse downstream effects on glucose metabolism through either direct regulation of glycolytic enzymes or the control of transcription factors (Hoxhaj and Manning, 2020). Constitutively active AKT has been shown to promote HK2 activity and indirectly stimulate phosphofructokinase 1 activity (Roberts et al., 2013). AKT phosphorylates and increases the activity of pyruvate dehydrogenase kinase 1 (Chae et al., 2016). PI3K/AKT signaling also mediates hypoxia-inducible factor 1 (Arsham et al., 2004), a key transcription factor in glycolysis. In addition, *Furin* and *MMPs* expressions are increased in *Slc45a2*-deficient cells, which promotes melanoma metastasis (Figure 6b). Furin is a multifunctional protease that has a conserved His69 site to sense an acidic pH environment for function (Feliciangeli et al., 2006). Acidified intracellular pH might elucidate the reason why furin expression is upregulated in *Slc45a2*-deficient cells (Figure 2a). MMPs are responsible for the remodeling of the extracellular matrix, which leads to melanoma invasion and metastasis (Bartolomé et al., 2009). Acidic extracellular pH induces cellular expression of *MMPs* and induces epithelial-mesenchymal transition changes in melanoma (Thakur and Bedogni, 2016). Because extracellular acidification is primarily considered to be caused by lactate secretion from anaerobic glycolysis, we found that the m+3 isotopologue of lactate from KO culture medium is significantly higher than that from WT medium (Figure 3f), which supports the proposed mechanism that *Slc45a2* deficiency will lead to more acidic intracellular pH to promote furin activity and further exacerbate extracellular pH by secreting lactate to activate MMP expressions.

In summary, our study sheds light on how SLC45A2 regulates glucose metabolism to influence melanin synthesis and melanoma metastasis, particularly discovering the glycolytic function of melanosomes. Selective restoration of *Slc45a2* function could rescue the symptom of albinism and serve as an effective strategy for melanoma therapy.

MATERIALS AND METHODS

Mice

WT and *Slc45a2*-KO mice were generated using CRISPR/Cas9 technology in C57BL/6J genetic background, as described in Supplementary Materials and Methods. All animal protocols were approved by the Institutional Animal Care and Use Committee of Tsinghua University (Beijing, China) and the Laboratory Animal Research Center of Tsinghua University.

Cell culture and murine PMC isolation

Melanoma cell line B16F10 was purchased from ATCC (Manassas, VA) and cultured in DMEM. WT and *Slc45a2*-KO PMCs were cultured in modified Ham's F12 medium. Detailed methods are described in Supplementary Materials and Methods.

Gene KO of *Slc45a2* in the B16F10 cell line

Two single-guide RNA sequences targeting were constructed with PX458-pSpCas9 (BB)-2A-GFP-MCS plasmid (a gift of Wei Guo); the procedures were based on the protocol from Zhang Feng's laboratory, as described in Supplementary Materials and Methods.

RNA extraction and RT-qPCR analysis

Total RNA was extracted from cells with HiPure Total RNA Plus Mini Kit (Magen Biotechnology, Guangzhou, China), and cDNA was reverse transcribed with FastQuant RT kit (Tiangen Biotech, Beijing, China). RT-qPCR was performed with TransStart Green qPCR SuperMix (TransGen Biotech, Beijing, China) and the gene primers (Supplementary Table S6) in 7500 Real-Time PCR Systems (Applied Biosystems, Waltham, MA).

Melanosome isolation

The detailed isolation method for functional melanosomes was modified as previously described (Pelkonen et al., 2016; Watabe et al., 2005). Detailed methods are provided in Supplementary Materials and Methods.

[U-$^{13}C_6$] glucose metabolic flux analysis

Briefly, cells were grown in a medium with or without [U-$^{13}C_6$] glucose for 12 hours, and the metabolites were extracted from media and cells with cold 80% methanol for the liquid chromatography-MS.

Data availability statement

No datasets were generated or analyzed during this study.

ORCIDs

Ye Liu: http://orcid.org/0000-0002-1901-669X
Wenna Chi: http://orcid.org/0000-0003-1922-5616
Lei Tao: http://orcid.org/0000-0002-6891-5608
Guoqiang Wang: http://orcid.org/0000-0003-4175-3837
R.N.V. Krishna Deepak: http://orcid.org/0000-0001-6629-8450
Linlin Sheng: http://orcid.org/0000-0001-5848-2290
Taiqi Chen: http://orcid.org/0000-0001-5670-112X
Yaqian Feng: http://orcid.org/0000-0002-0566-1188
Xizhi Cao: http://orcid.org/0000-0002-5496-1304
Lili Cheng: http://orcid.org/0000-0001-8009-1069
Xinbin Zhao: http://orcid.org/0000-0002-6242-017X
Xiaohui Liu: http://orcid.org/0000-0001-7391-5058
Haiteng Deng: https://orcid.org/0000-0001-9496-1280
Hao Fan: http://orcid.org/0000-0003-0199-9752
Peng Jiang: http://orcid.org/0000-0002-4218-0092
Ligong Chen: http://orcid.org/0000-0002-7893-7173

CONFLICT OF INTEREST

The authors state no conflict of interest.

ACKNOWLEDGMENTS

We greatly thank our colleagues Bao-Liang Song at Wuhan University (Wuhan, China) for very helpful discussion on glycosome and Yi Ding at Tsinghua University (Beijing, China) for high-performance liquid chromatography-mass spectrometry experiments. We are also thankful for the support of the animal core facility at Tsinghua University. This work was supported by the National Natural Science Foundation of China (32130048, 92157301, 31971085, and 91857108 to LChen), Ministry of Science and Technology of China National Key R&D Programs (2018YFA0506903 to LChen), Nation Science and Technology Major Projects for Major New Drugs Innovation and Development (2018ZX09711003-004-002 to LChen), Tsinghua University Spring Breeze Fund (2021Z99CFY012 to LChen), and Tsinghua-Foshan Innovation Special Fund (2020THFS0133 to LChen).

AUTHOR CONTRIBUTIONS

Conceptualization: LChen; Data Curation: YL, LChen; Formal Analysis: YL, WC, LT, GW, XZ, LChen; Funding Acquisition: LChen; Investigation: YL, WC, LT, GW, XC, YF, LCheng, XZ, LChen; Methodology: YL, WC, LS, RNVKD, TC, HF, XL, HD, PJ, LChen; Supervision: HF, PJ, LChen; Visualization: YL, WC, LT, RNVKD, HF, LChen; Writing - Original Draft Preparation: YL, WC, LChen; Writing - Review and Editing: YL, WC, HF, LChen

SUPPLEMENTARY MATERIAL

Supplementary material is linked to the online version of the paper at www.jidonline.org, and at https://doi.org/10.1016/j.jid.2022.04.008.

REFERENCES

Adelmann CH, Traunbauer AK, Chen B, Condon KJ, Chan SH, Kunchok T, et al. MFSD12 mediates the import of cysteine into melanosomes and lysosomes. Nature 2020;588:699–704.

Ambrosio AL, Boyle JA, Aradi AE, Christian KA, Di Pietro SM. TPC2 controls pigmentation by regulating melanosome pH and size. Proc Natl Acad Sci USA 2016;113:5622–7.

Ancans J, Tobin DJ, Hoogduijn MJ, Smit NP, Wakamatsu K, Thody AJ. Melanosomal pH controls rate of melanogenesis, eumelanin/phaeomelanin ratio and melanosome maturation in melanocytes and melanoma cells. Exp Cell Res 2001;268:26–35.

Arsham AM, Plas DR, Thompson CB, Simon MC. Akt and hypoxia-inducible factor-1 independently enhance tumor growth and angiogenesis. Cancer Res 2004;64:3500–7.

Ashkenazy H, Abadi S, Martz E, Chay O, Mayrose I, Pupko T, et al. ConSurf 2016: an improved methodology to estimate and visualize evolutionary conservation in macromolecules. Nucleic Acids Res 2016;44:W344–50.

Bartölke R, Heinisch JJ, Wieczorek H, Vitavska O. Proton-associated sucrose transport of mammalian solute carrier family 45: an analysis in Saccharomyces cerevisiae. Biochem J 2014;464:193–201.

Bartolomé RA, Ferreiro S, Miquilena-Colina ME, Martínez-Prats L, Soto-Montenegro ML, García-Bernal D, et al. The chemokine receptor CXCR4 and the metalloproteinase MT1-MMP are mutually required during melanoma metastasis to lungs. Am J Pathol 2009;174:602–12.

Bellono NW, Escobar IE, Lefkovith AJ, Marks MS, Oancea E. An intracellular anion channel critical for pigmentation. Elife 2014;3:e04543.

Bin BH, Kim ST, Bhin J, Lee TR, Cho EG. The development of sugar-based anti-melanogenic agents. Int J Mol Sci 2016;17:583.

Boukouris AE, Zervopoulos SD, Michelakis ED. Metabolic enzymes moonlighting in the nucleus: metabolic regulation of gene transcription. Trends Biochem Sci 2016;41:712–30.

Chae YC, Vaira V, Caino MC, Tang HY, Seo JH, Kossenkov AV, et al. Mitochondrial Akt regulation of hypoxic tumor reprogramming. Cancer Cell 2016;30:257–72.

Chen L, Shu Y, Liang X, Chen EC, Yee SW, Zur AA, et al. OCT1 is a high-capacity thiamine transporter that regulates hepatic steatosis and is a target of metformin. Proc Natl Acad Sci USA 2014;111:9983–8.

Chiaverini C, Sillard L, Flori E, Ito S, Briganti S, Wakamatsu K, et al. Cystinosin is a melanosomal protein that regulates melanin synthesis. FASEB J 2012;26:3779–89.

Chintala S, Li W, Lamoreux ML, Ito S, Wakamatsu K, Sviderskaya EV, et al. Slc7a11 gene controls production of pheomelanin pigment and proliferation of cultured cells. Proc Natl Acad Sci USA 2005;102:10964–9.

Crawford NG, Kelly DE, Hansen MEB, Beltrame MH, Fan S, Bowman SL, et al. Loci associated with skin pigmentation identified in African populations [published correction appears in Science 2020;367:eaba7178]. *Science* 2017;358:eaan8433.

Dankort D, Curley DP, Cartlidge RA, Nelson B, Karnezis AN, Damsky WE Jr, et al. Braf(V600E) cooperates with Pten loss to induce metastatic melanoma. Nat Genet 2009;41:544–52.

Davies LC, Rice CM, Palmieri EM, Taylor PR, Kuhns DB, McVicar DW. Peritoneal tissue-resident macrophages are metabolically poised to engage microbes using tissue-niche fuels. Nat Commun 2017;8:2074.

Diallinas G. Understanding transporter specificity and the discrete appearance of channel-like gating domains in transporters. Front Pharmacol 2014;5:207.

Feliciangeli SF, Thomas L, Scott GK, Subbian E, Hung CH, Molloy SS, et al. Identification of a pH sensor in the furin propeptide that regulates enzyme activation. J Biol Chem 2006;281:16108–16.

Fernandez LP, Milne RL, Pita G, Avilés JA, Lázaro P, Benítez J, et al. SLC45A2: a novel malignant melanoma-associated gene. Hum Mutat 2008;29:1161–7.

Ganapathy V, Thangaraju M, Prasad PD. Nutrient transporters in cancer: relevance to Warburg hypothesis and beyond. Pharmacol Ther 2009;121:29–40.

Gaudel C, Soysouvanh F, Leclerc J, Bille K, Husser C, Montcriol F, et al. Regulation of melanogenesis by the amino acid transporter SLC7A5. J Invest Dermatol 2020;140:2253–9.e4.

Guedj M, Bourillon A, Combadières C, Rodero M, Dieudé P, Descamps V, et al. Variants of the MATP/SLC45A2 gene are protective for melanoma in the French population. Hum Mutat 2008;29:1154–60.

Haanstra JR, González-Marcano EB, Gualdrón-López M, Michels PA. Biogenesis, maintenance and dynamics of glycosomes in trypanosomatid parasites. Biochim Biophys Acta 2016;1863:1038–48.

Hoxhaj G, Manning BD. The PI3K-AKT network at the interface of oncogenic signalling and cancer metabolism. Nat Rev Cancer 2020;20:74–88.

Inagaki K, Suzuki T, Ito S, Suzuki N, Adachi K, Okuyama T, et al. Oculocutaneous albinism type 4: six novel mutations in the membrane-associated transporter protein gene and their phenotypes. Pigment Cell Res 2006;19:451–3.

Jumper J, Evans R, Pritzel A, Green T, Figurnov M, Ronneberger O, et al. Highly accurate protein structure prediction with AlphaFold. Nature 2021;596:583–9.

Kwong LN, Davies MA. Navigating the therapeutic complexity of PI3K pathway inhibition in melanoma. Clin Cancer Res 2013;19:5310–9.

Le L, Escobar IE, Ho T, Lefkovith AJ, Latteri E, Haltaufderhyde KD, et al. SLC45A2 protein stability and regulation of melanosome pH determine melanocyte pigmentation. Mol Biol Cell 2020;31:2687–702.

Lee SH, Bae IH, Lee ES, Kim HJ, Lee J, Lee CS. Glucose exerts an anti-melanogenic effect by indirect inactivation of tyrosinase in melanocytes and a human skin equivalent. Int J Mol Sci 2020;21:1736.

Meyer H, Vitavska O, Wieczorek H. Identification of an animal sucrose transporter. J Cell Sci 2011;124:1984–91.

Park J, Talukder AH, Lim SA, Kim K, Pan K, Melendez B, et al. SLC45A2: a melanoma antigen with high tumor selectivity and reduced potential for autoimmune toxicity. Cancer Immunol Res 2017a;5:618–29.

Park TJ, Reznick J, Peterson BL, Blass G, Omerbašić D, Bennett NC, et al. Fructose-driven glycolysis supports anoxia resistance in the naked mole-rat. Science 2017b;356:307–11.

Pelkonen L, Reinisalo M, Morin-Picardat E, Kidron H, Urtti A. Isolation of intact and functional melanosomes from the retinal pigment epithelium. PLoS One 2016;11:e0160352.

Perland E, Bagchi S, Klaesson A, Fredriksson R. Characteristics of 29 novel atypical solute carriers of major facilitator superfamily type: evolutionary conservation, predicted structure and neuronal co-expression. Open Biol 2017;7:170142.

Reddy VS, Shlykov MA, Castillo R, Sun EI, Saier MH Jr. The major facilitator superfamily (MFS) revisited [published correction appears in FEBS J 2013;280:3975]. FEBS J 2012;(279):2022–35.

Reinders A, Ward JM. Investigating polymorphisms in membrane-associated transporter protein SLC45A2, using sucrose transporters as a model. Mol Med Rep 2015;12:1393–8.

Roberts DJ, Tan-Sah VP, Smith JM, Miyamoto S. Akt phosphorylates HK-II at Thr-473 and increases mitochondrial HK-II association to protect cardiomyocytes [published correction appears in J Biol Chem 2013;288:32638]. J Biol Chem 2013;(288):23798–806.

Smith DR, Spaulding DT, Glenn HM, Fuller BB. The relationship between Na(+)/H(+) exchanger expression and tyrosinase activity in human melanocytes. Exp Cell Res 2004;298:521–34.

Thakur V, Bedogni B. The membrane tethered matrix metalloproteinase MT1-MMP at the forefront of melanoma cell invasion and metastasis. Pharmacol Res 2016;111:17–22.

Vitavska O, Wieczorek H. The SLC45 gene family of putative sugar transporters. Mol Aspects Med 2013;34:655–60.

Vitavska O, Wieczorek H. Putative role of an SLC45 H+/sugar cotransporter in mammalian spermatozoa. Pflugers Arch 2017;469:1433–42.

Watabe H, Kushimoto T, Valencia JC, Hearing VJ. Isolation of melanosomes. Curr Protoc Cell Biol 2005. Chapter:Unit 3.14.

Wei AH, Zang DJ, Zhang Z, Liu XZ, He X, Yang L, et al. Exome sequencing identifies SLC24A5 as a candidate gene for nonsyndromic oculocutaneous albinism. J Invest Dermatol 2013;133:1834–40.

Zhang Y, Zhang Y, Sun K, Meng Z, Chen L. The SLC transporter in nutrient and metabolic sensing, regulation, and drug development. J Mol Cell Biol 2019;11:1–13.

This work is licensed under a Creative Commons Attribution-NonCommercial-NoDerivatives 4.0 International License. To view a copy of this license, visit http://creativecommons.org/licenses/by-nc-nd/4.0/

SUPPLEMENTARY MATERIALS AND METHODS

Chemicals and reagents

Bafilomycin A1 (HY-100558), 5-N, N-hexamethylene amiloride (HY-128067), UK5099 (HY-15475), and GSK2837808A (HY-100681) were purchased from MedChemExpress (Monmouth Junction, NJ); 2-deoxy-D-glucose was purchased from Apexbio Technology (Houston, TX) (B1027); [^{14}C(U)]-sucrose (NEC100X250UC) and 2-[1,2-^{3}H (N)]-deoxy-D-glucose (NET328A250UC) were purchased from PerkinElmer (Waltham, MA); L-lactate (L6402), sodium lactate (71718), tamoxifen (T5648), and 4-hydroxytamoxifen (H6278) were purchased from Sigma-Aldrich (St. Louis, MO); and 4-amino-3-hydroxyphenylalanine was synthesized as previously reported (Wakamatsu et al., 2002).

Plasmid construction

Melanosome-localized pH sensor plasmid was a gift from Santiago Di Pietro (plasmid number 80151, Addgene, Watertown, MA). Using human SLC45A2 and mouse SLC45A2 cDNA as templates, genes were cloned into pcDNA5/FRT vector (Invitrogen, Waltham, MA). Adenovirus for overexpressing 6His-tagged SLC45A2 was packaged as previously described (He et al., 1998). Flag-tagged SLC45A2 and TYRP1 were cloned into pCMV6-Entry construct (OriGene, Rockville, MD). All constructs used in this study were confirmed by sequencing.

Generation of *Slc45a2*-deficient mice

Generation of *Slc45a2*-knockout mice was done using CRISPR/Cas9 system in C57BL/6 zygotes. The candidate chimeric single-guide RNA (sgRNA) targeting exon 1 of *Slc45a2* (National Center for Biotechnology Information sequence NM_053077) was designed on the basis of http://crispr.mit.edu/. sgRNA and humanized Cas9 mRNA were transcripted respectively using the MEGAshortscript kit (Am1354, Ambion, Austin, TX) and mMESSAGE mMACHINE T7 Ultra Kit (Am1345, Ambion) according to the manufacturer's instructions. Both the sgRNA and the Cas9 mRNA were purified using the MEGAclear kit (AM1908, Ambion). The sgRNA (30 ng/μl) was mixed with Cas9 mRNA (60 ng/μl), and the mixture was microinjected into the cytoplasm of the one-cell stage embryos. Genomic DNA was extracted from the tail tips of the newborn pups, and the genomic sequences around the sgRNA target sites were PCR amplified using the following primers: forward primer 5′-AGCGTGGGCCTGCCTAAGAGC-3′ and reverse primer 5′-CCACTTACCTGATACGACCGCATCTC-3′.

Cell culture and murine primary melanocytes isolation

Melanoma cell line B16F10 was purchased from ATCC (Manassas, VA) and cultured in DMEM, supplemented with 10% fetal bovine serum and 1% streptomycin and penicillin at 37 °C with 5% carbon dioxide. Wild-type and *Slc45a2*-knockout primary melanocytes were cultured in modified Ham's F12 medium as previously reported (Costin et al., 2003). Briefly, the dorsal skins were derived from C57BL/6J mice aged 1 day and were soaked with iodine solution, 75% ethanol, and PBS for 3 minutes. Then, the dissected skins were incubated in 0.25% trypsin at 37 °C for 3 hours. The epidermis was separated from the dermis and removed into a 6-cm dish. We cut the epidermis into small pieces and added 2 ml of 0.25% trypsin at 37% for 2 minutes. We stopped the digestion by adding 4 ml Ham's F12 medium containing 10% fetal bovine serum, 0.1 mM 3-isobutyl-1-methylxanthine (Sigma-Aldrich), 10 μg/ml bovine pituitary extract (Sciencell Research Laboratories, Carlsbad, CA), 48 nM 12-O-Tetradecanoylphorbol 13-acetate (Beyotime Biotechnology, Jiangsu, China), 0.5 mM GlutaMax (Gibco, Waltham, MA), and 1% streptomycin/penicillin.

Gene knockout of *Slc45a2* in the B16F10 cell line

Two sgRNA sequences targeting were constructed with PX458-pSpCas9 (BB)-2A-GFP-MCS plasmid (a gift of Wei Guo); the procedures were based on the protocol from Zhang Feng's laboratory (Ran et al., 2013). Briefly, a pair of oligos were annealed, phosphorylated, and ligated to the linearized vector. The oligos sequences are as follows: 5′-GTCGAAGGAGTTTTGAGCCAC-3′ and 5′-TCACCATTCACAGGTCCGTC-3′. Cells were sorted in 96-well plates using FACS with a FACSAria II cell sorter (BD Biosciences, San Jose, CA) after transfection. Single-cell colonies were obtained, and we extracted the genomic DNA for further genotyping PCR and sequencing.

Lentiviral short-hairpin RNA knockdown system

The lentiviral system was generated as previously described (Moffat et al., 2006). The oligonucleotides (Invitrogen) were annealed and subcloned into the lentiviral vector pLKO.1. The lentiviruses were generated by transfecting human embryonic kidney 293T cells together with the lentiviral Vesicular stomatitis virus G and psPAX2 plasmids (plasmid numbers 12259 and 12260, Addgene). The viral supernatants were collected after 48 hours and then infected into cells. The knockdown efficiency of the target genes was determined by western blotting or RT-PCR. The oligonucleotide sequences for the pLKO.1 short-hairpin RNAs are listed in Supplementary Table S6.

Melanin content and pheomelanin measurement

The total melanin content was measured using a reported method modified from the study by Bellono et al. (2016). Briefly, cells were harvested in PBS/1% Triton X-100 by collection with a cell scraper and lysed at 4 °C for 30 minutes, and the insoluble fraction was obtained by centrifugation at 12,000 r.p.m. for 15 minutes and was dissolved in 1 N sodium hydroxide for 2 hours at 85 °C to measure the absorbance at 405 nm. The cellular melanin values were expressed as milligram melanin per milligram protein.

The whole dorsal skin of mice aged 3 months was collected for pheomelanin measurement. Using high-performance liquid chromatography, pheomelanin was analyzed on the basis of the levels of 4-amino-3-hydroxyphenylalanine produced by hydriodic acid hydrolysis (Ito and Wakamatsu, 1994; Thody et al., 1991) (Supplementary Figure S2d).

Tyrosinase activity

Tyrosinase activity was assayed using a Tyrosinase Activity Assay Kit (catalog number K742, Biovision, Milpitas, CA) following the instructions of the manufacturer.

Structural modeling

We constructed the structural models of the mouse and human *SLC45A2* using the Robetta protein structure prediction

webserver employing the comparative modeling method (Kim et al., 2004). Both the mouse and human models were modeled in the inward-open conformation and were structurally most similar to the xylose-bound proton:xylose symporter XylE from *E. coli* (PDB identification 4GBY) (Sun et al., 2012).

Melanosomal pH measurement

When the cell reached 80% confluence, the medium was removed from the dish, and we added the 1 μM prewarmed (37 °C) probe LysoSensor Green DND-189 (Yeason, Shanghai, China) in Hank's balanced salt solution buffer. We incubated the cells in the dark for 30 minutes at 37 °C. Cells were digested with 0.25% trypsin/EDTA and resuspended in 500 μl of Hank's balanced salt solution for flow cytometer (BD Calibur, Sparks, NV). A total of 2 μg melanosome-localized pH sensor plasmid was transfected in a six-well plate. Cells were digested and collected in 500 μl of Hank's balanced salt solution for flow cytometer after 48 hours of transfection or seeded in a 35-mm confocal dish.

Glycolytic enzyme activity

Hexokinase activity was measured using a hexokinase activity assay kit (Solarbio Life Science, Beijing, China) according to the manufacturer's instructions. Pyruvate kinase activity assay was measured by a lactate dehydrogenase-coupled enzyme assay. The assay was carried out with purified melanosome lysates with an enzyme buffer (50 mM Tris-hydrogen chloride, 100 mM potassium chloride, 10 mM magnesium chloride, 1 mM adenosine diphosphate, 1 mM phosphoenolpyruvate, 1 mM nicotinamide adenine dinucleotide, and 4.8 U/ml lactate dehydrogenase). The decrease in absorbance at 340 nm from the oxidation of nicotinamide adenine dinucleotide was measured by a microplate reader. Lactate dehydrogenase activity assay was measured with purified melanosomes with the enzyme buffer (50 mM Tris-hydrogen chloride, 1 mM sodium pyruvate, 1 mM nicotinamide adenine dinucleotide, pH 7.6). The decrease in absorbance at 340 nm from the oxidation of nicotinamide adenine dinucleotide was measured by a microplate reader.

RNA-sequencing data analysis

RNA-sequencing reads were aligned to mouse transcriptome (UCSC gene) and genome (GRCm38/mm10) references, using the HISAT and Bowtie 2 software. After the library alignment and quality filter steps, the reads count values were obtained and used to calculate the fragments per kilobase of exon per million fragments mapped of the transcripts from different groups, considering the statistical significance of the differential gene expressions.

Western immunoblotting

Tissues and cells were rinsed with PBS and lysed in radioimmunoprecipitation assay lysis buffer (Beyotime Biotechnology, Shanghai, China) with cOmplete Protease Inhibitor Cocktail Tablets (Roche, Mannheim, Germany) and InStab Phosphatase Inhibitor Cocktail (Yeason). The primary antibodies used in this study were as followed: anti-β-actin (30102ES40, Yeason), anti-6His (30402ES40, Yeason), and anti-TYRP1 (NBP2-32906, Novus Biologicals, Littleton, CO). Anti-β-catenin (sc-7963), anti- glycogen synthase kinase-3β (sc-377213), and antiphosphorylated glycogen synthase kinase-3β (S9, sc-373800) were purchased from Santa Cruz Biotechnology (Dallas, TX). The anti-Flag (ab205606), anti-tyrosinase (ab170905), and anti-SLC2A1 (ab115730) were purchased from Abcam (Cambridge, United Kingdom). The anti-hexokinase 1 (2024T), anti-hexokinase 2 (2867T), anti-GAPDH (5174T), anti-pyruvate kinase 1/2 (3106S), anti-pyruvate kinase M2 (4053T), anti-pyruvate dehydrogenase (3205T), antiphosphorylated AMPKA (T172, 2535T), anti-lactate dehydrogenase (3582T), anti-Tomm20 (42406S), antiphosphorylated phosphatidylinositol 3-kinase (4228), anti-protein kinase B (4691), antiphosphorylated protein kinase B (S473, 4060), and c-Myc (5605) were purchased from Cell Signaling Technology (Danvers, MA).

Coimmunoprecipitation

Cell lysates derived from human embryonic kidney 293T transiently transfected with plasmids were prepared using a lysis buffer containing 50 mM Tris-hydrogen chloride, pH 7.4, 150 mM sodium chloride, 0.2% NP-40, 0.1% dodecyl maltoside, 10% glycerol, and protease inhibitor cocktail (Roche). The anti-flag magnetic beads (B26101, Bimake.com, Houston, TX) or the anti-His affinity gel (20589ES03, Yeason) was incubated with cell lysates at 4 °C overnight on a rotating wheel and subsequently washed five times with lysis buffer. The immunoprecipitated proteins were eluted with 1× SDS loading buffer.

Glucose consumption and lactate production

Glucose consumption was calculated by measuring the glucose concentration in a culture medium from blank and cell-seeded wells with a Glucose Consumption Assay Kit (E1010, Applygen, Beijing, China). Extracellular lactate was quantified in cell culture supernatants using the L-Lactate Assay Kit (Eton Bioscience, San Diego, CA) according to manufacturer's instructions.

Assay for transposase-accessible chromatin using sequencing

Assay for transposase-accessible chromatin using sequencing was performed as described before (Buenrostro et al., 2013). Nuclei isolated from 50,000 counted melanocytes were harvested at 500*g* for 5 minutes at 4 °C, and cell pellets were resuspended in 100 μl lysis buffer (10 mM Tris- hydrogen chloride, pH 7.4, 10 mM sodium chloride, 3 mM magnesium chloride, 0.5% NP-40) and then centrifuged at 500*g* for 15 minutes at 4 °C. The nuclei were resuspended in the transposition reaction mixture with Tn5 transposase (Vazyme Biotech, Nanjing, China) on ice and then incubated for 30 minutes at 37 °C. The transposed DNA was purified using the MinElute kit (Qiagen, Hilden, Germany) and amplified in 50 μl PCR reactions using primers with unique barcodes (Vazyme Biotech) and then selected using AMPureXP beads (Agencourt, Beckman Coulter, Brea, CA) to setup library. The library was sequenced using Illumina HiSeq X Ten sequencer by Novogene (Beijing, China) to obtain 150 base pair paired-end reads.

Melanosome isolation

The detailed isolation method for functional melanosomes was modified as previously described (Pelkonen et al., 2016; Watabe et al., 2005). Briefly, at least 1 × 10^8 cells were harvested, homogenized on ice, and centrifuged, and the supernatant was separated by a 2.0 M sucrose

density gradient (from top to bottom: 1.0, 1.2, 1.4, 1.5, 1.6, 1.8, and 2.0 M) in a 38.5 ml polyallomer centrifuge tube (number 344058, Beckman Coulter, Brea, CA). Centrifugation was performed in an SW 32 Ti swinging bucket rotor in Beckman L-100XP at 135,000*g* for 1 hour at 4 °C. After centrifugation, all the upper layers were discarded, and the purified melanosomal pellet was resuspended in 2-morpholinoethanesulfonic acid buffer (25 mM 2-morpholinoethanesulfonic acid, 5 mM sodium chloride, 115 mM potassium chloride, 1.3 mM magnesium sulfate, pH 7.4). The remaining sucrose gradient was removed by centrifugation at 10,000*g* for 5 minutes at 4 °C, and the melanosomal pellet was kept.

In vivo tumor models

Melanoma cells (300,000 cells in 100 μl of PBS) were injected subcutaneously into the dorsal region of nude mice, and the metastatic model was induced by injecting 300,000 melanoma cells in 100 μl of PBS in the tail vein of nude mice. After 14 days, the mice were euthanized, and tumors and lungs were collected for further experiments.

Activation of *Braf*/*Pten*/*Tyr*^{Cre} transgene melanoma mice

Topical administration of 4-hydroxytamoxifen was performed by preparing a 25 mg/ml stock solution of 4-hydroxytamoxifen in DMSO. For localized melanoma induction on the back skin, adult mice aged 4 weeks were shaved and treated topically with 10 μl of 1.55 mg/ml of 4-hydroxytamoxifen for 3 consecutive days. Generalized induction in adult mice aged 4 weeks was conducted by intraperitoneal injection of 150 μl of 10 mg/ml tamoxifen suspension in corn oil on 3 consecutive days.

Statistical analysis

GraphPad Prism 6 software (GraphPad Software, San Diego, CA) was utilized for statistical analysis. All data were expressed as mean ± SD or mean ± SEM. Student's *t*-tests or two-way ANOVA followed by Tukey's multiple comparison tests were performed for the indicated comparisons ($*P < 0.05$, $**P < 0.01$, and $***P < 0.001$).

SUPPLEMENTARY REFERENCES

Bellono NW, Escobar IE, Oancea E. A melanosomal two-pore sodium channel regulates pigmentation. Sci Rep 2016;6:26570.

Buenrostro JD, Giresi PG, Zaba LC, Chang HY, Greenleaf WJ. Transposition of native chromatin for fast and sensitive epigenomic profiling of open chromatin, DNA-binding proteins and nucleosome position. Nat Methods 2013;10:1213–8.

Costin GE, Valencia JC, Vieira WD, Lamoreux ML, Hearing VJ. Tyrosinase processing and intracellular trafficking is disrupted in mouse primary melanocytes carrying the underwhite (uw) mutation. A model for oculocutaneous albinism (OCA) type 4. J Cell Sci 2003;116(Pt 15):3203–12.

He TC, Zhou S, da Costa LT, Yu J, Kinzler KW, Vogelstein B. A simplified system for generating recombinant adenoviruses. Proc Natl Acad Sci U S A 1998;95:2509–14.

Ito S, Wakamatsu K. An improved modification of permanganate oxidation of eumelanin that gives a constant yield of pyrrole-2,3,5-tricarboxylic acid. Pigment Cell Res 1994;7:141–4.

Kim DE, Chivian D, Baker D. Protein structure prediction and analysis using the Robetta server. Nucleic Acids Res 2004;32:W526–31.

Moffat J, Grueneberg DA, Yang X, Kim SY, Kloepfer AM, Hinkle G, et al. A lentiviral RNAi library for human and mouse genes applied to an arrayed viral high-content screen. Cell 2006;124:1283–98.

Pelkonen L, Reinisalo M, Morin-Picardat E, Kidron H, Urtti A. Isolation of intact and functional melanosomes from the retinal pigment epithelium. PLoS One 2016;11:e0160352.

Ran F, Hsu P, Wright J, Agarwala V, Scott DA, Zhang F. Genome engineering using the CRISPR-Cas9 system. Nat Protoc 2013;8:2281–308.

Sun L, Zeng X, Yan C, Sun X, Gong X, Rao Y, et al. Crystal structure of a bacterial homologue of glucose transporters GLUT1-4. Nature 2012;490:361–6.

Thody AJ, Higgins EM, Wakamatsu K, Ito S, Burchill SA, Marks JM. Pheomelanin as well as eumelanin is present in human epidermis. J Invest Dermatol 1991;97:340–4.

Wakamatsu K, Ito S, Rees JL. The usefulness of 4-amino-3-hydroxyphenylalanine as a specific marker of pheomelanin. Pigment Cell Res 2002;15:225–32.

Watabe H, Kushimoto T, Valencia JC, Hearing VJ. Isolation of melanosomes. Curr Protoc Cell Biol 2005. Chapter:Unit 3.14.

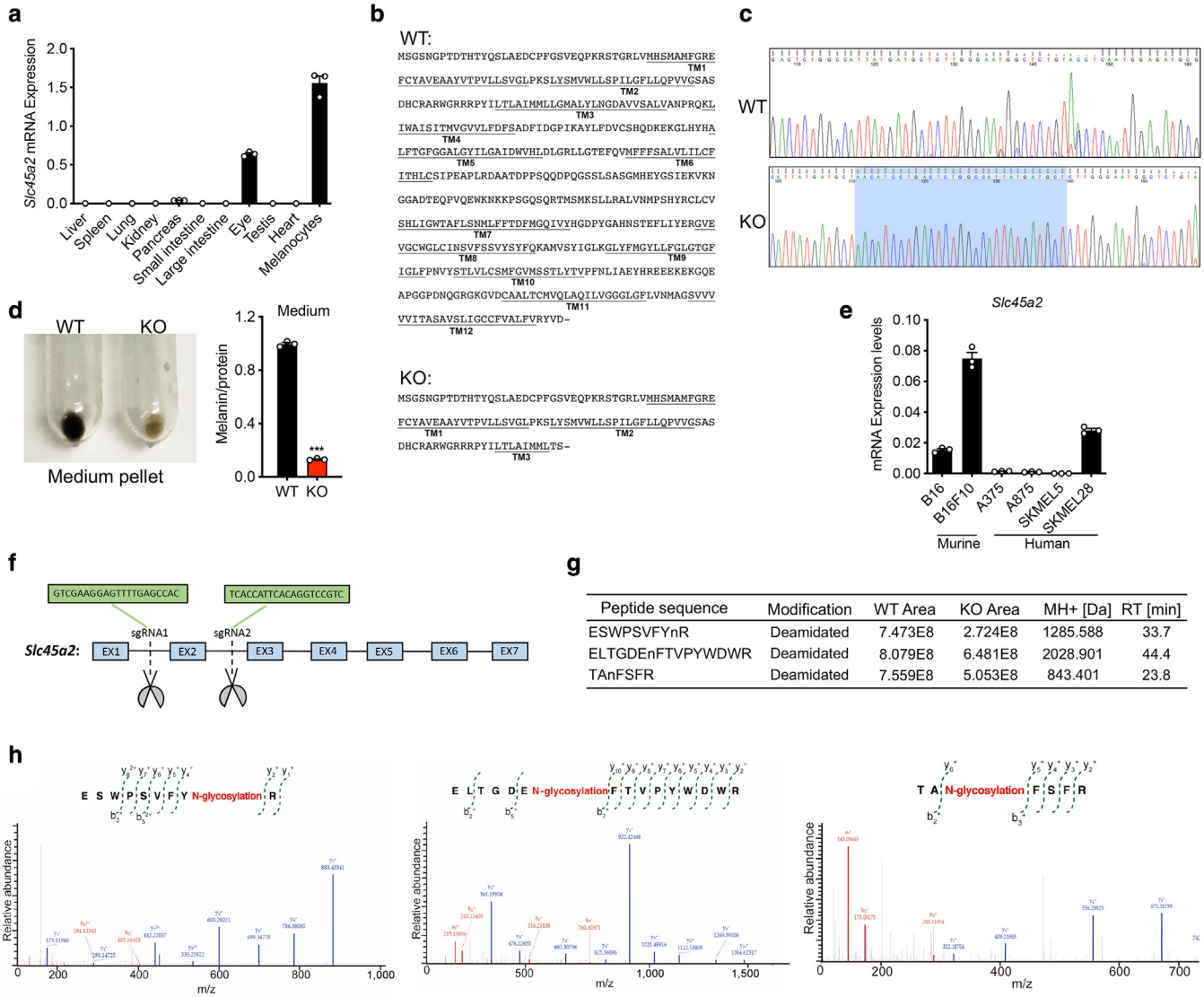

Peptide sequence	Modification	WT Area	KO Area	MH+ [Da]	RT [min]
ESWPSVFYnR	Deamidated	7.473E8	2.724E8	1285.588	33.7
ELTGDEnFTVPYWDWR	Deamidated	8.079E8	6.481E8	2028.901	44.4
TAnFSFR	Deamidated	7.559E8	5.053E8	843.401	23.8

Supplementary Figure S1. Generation of *Slc45a2*-KO models and detection of tyrosinase glycosylation by MS. **(a)** Expression levels of *Slc45a2* in different murine tissues and melanocytes (n = 3). **(b)** Protein sequences of WT and *Slc45a2*-KO mice. TM represents the TM domain. *Slc45a2*-KO mice introduce a premature stop codon in the TM3. **(c)** Genomic DNA sequences of WT and *Slc45a2*-KO mice; incorrect genomic DNA sequence in exon 1 was highlighted. **(d)** Melanin content of medium pellet collected from *Slc45a2*-KO melanocytes was significantly reduced compared with that from WT melanocytes (n = 3). **(e)** *Slc45a2* mRNA expression levels in different murine and human melanoma cells (n = 3). **(f)** Graphical illustration of deleting *Slc45a2* using CRISPR/Cas9 technology in B16F10 cells. sgRNA1 (5′-GTCGAAGGAGTTTTGAGCCAC-3′) and sgRNA2 (5′-TCACCATTCACAGGTCCGTC-3′) are on opposite sides of exon 2. **(g)** Peak areas of deamidated tyrosinase peptide sequences detected by MS. WT or KO area represents peptide abundance, MH+, and RT. **(h)** MS analysis to identify three glycosylation sites of tyrosinase and the MS spectra of representative peptides are presented. Data are shown as mean ± SEM. For **d**, Student's *t*-tests were used for the indicated comparisons. $*P < 0.05$, $**P < 0.01$, and $***P < 0.001$. EX, exon; KO, knockout; m/z, mass-to-charge ratio; MH+, mass-to-charge ratio; min, minute; MS, mass spectrometry; RT, retention time; sgRNA, single-guide RNA; TM, transmembrane; TM3, transmembrane domain 3; WT, wild type.

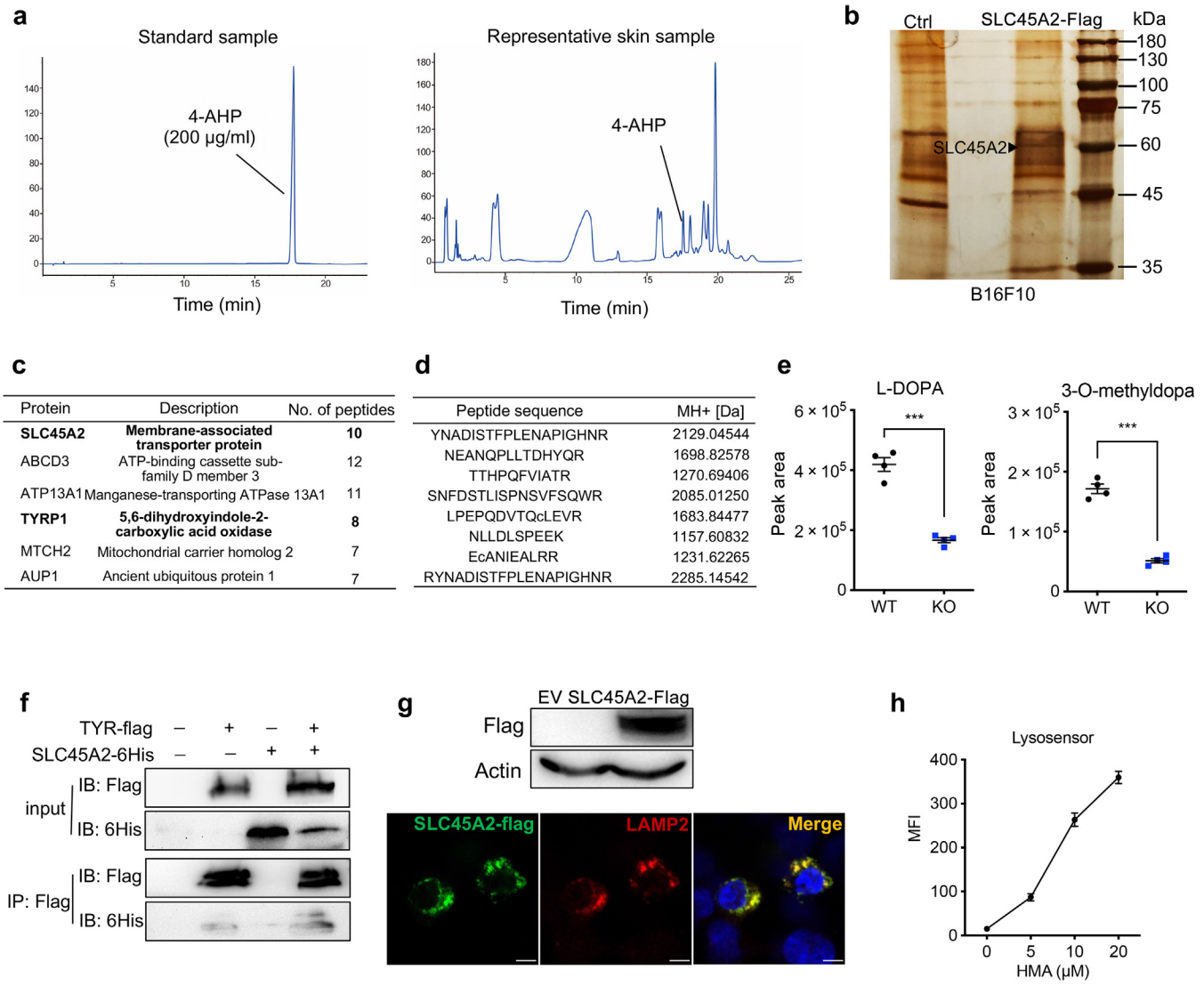

Protein	Description	No. of peptides
SLC45A2	**Membrane-associated transporter protein**	**10**
ABCD3	ATP-binding cassette sub-family D member 3	12
ATP13A1	Manganese-transporting ATPase 13A1	11
TYRP1	**5,6-dihydroxyindole-2-carboxylic acid oxidase**	**8**
MTCH2	Mitochondrial carrier homolog 2	7
AUP1	Ancient ubiquitous protein 1	7

Peptide sequence	MH+ [Da]
YNADISTFPLENAPIGHNR	2129.04544
NEANQPLLTDHYQR	1698.82578
TTHPQFVIATR	1270.69406
SNFDSTLISPNSVFSQWR	2085.01250
LPEPQDVTQcLEVR	1683.84477
NLLDLSPEEK	1157.60832
EcANIEALRR	1231.62265
RYNADISTFPLENAPIGHNR	2285.14542

Supplementary Figure S2. Pheomelaninmeasurement and identification of TYRP1 as interacted protein of SLC45A2. **(a)** Representative HPLC chromatograms of 4-AHP in standards and representative skin samples. **(b)** A representative silver staining gel of Flag Ctrl and Flag-tagged SLC45A2 (SLC45A2-Flag) samples. SLC45A2 protein band identified by mass spectrometry around 60 kDa is indicated with the arrowhead. **(c)** Identification of SLC45A2-interacting proteins in SLC45A2-Flag–overexpressed B16F10 cells. **(d)** Eight peptides of TRYP1 identified by mass spectrometry. **(e)** The abundances of L-DOPA and 3-O-methyldopa are measured by LC–MS in WT and *Slc45a2*-KO B16F10 cells. **(f)** Coimmunoprecipitation of *Slc45a2*-6His and Tyr-Flag in HEK293T cells. **(g)** Western blotting analysis of SLC45A2 protein level using Flag antibody in HEK293T cells overexpressing SLC45A2-Flag recombinant protein (up); subcellular colocalization between SLC45A2-Flag protein and lysosome marker LAMP2 in HEK293T cells (down). Bar = 10 μm. **(h)** Lysosomal pH was measured by MFI of Lysosensor Green DND-189 (lysosensor) in HEK293T cells treated with 0, 5, 10, or 20 μM HMA (n = 3). Data are shown as mean ± SEM. For **e**, Student's *t*-tests were used for the indicated comparisons. *$P < 0.05$, **$P < 0.01$, and ***$P < 0.001$. 4-AHP, 4-amino-3-hydroxyphenylalanine; Ctrl, control; EV, empty vector; HEK293T, human embryonic kidney 293T; HMA, 5-N, N-hexamethylene amiloride; HPLC, high-performance liquid chromatography; IB, immunoblotting; IP, immunoprecipitation; KO, knockout; LC–MS, liquid chromatography–mass spectrometry; L-DOPA, levodopa; MFI, mean fluorescence intensity; min, minute; Tyr, tyrosinase; WT, wild type.

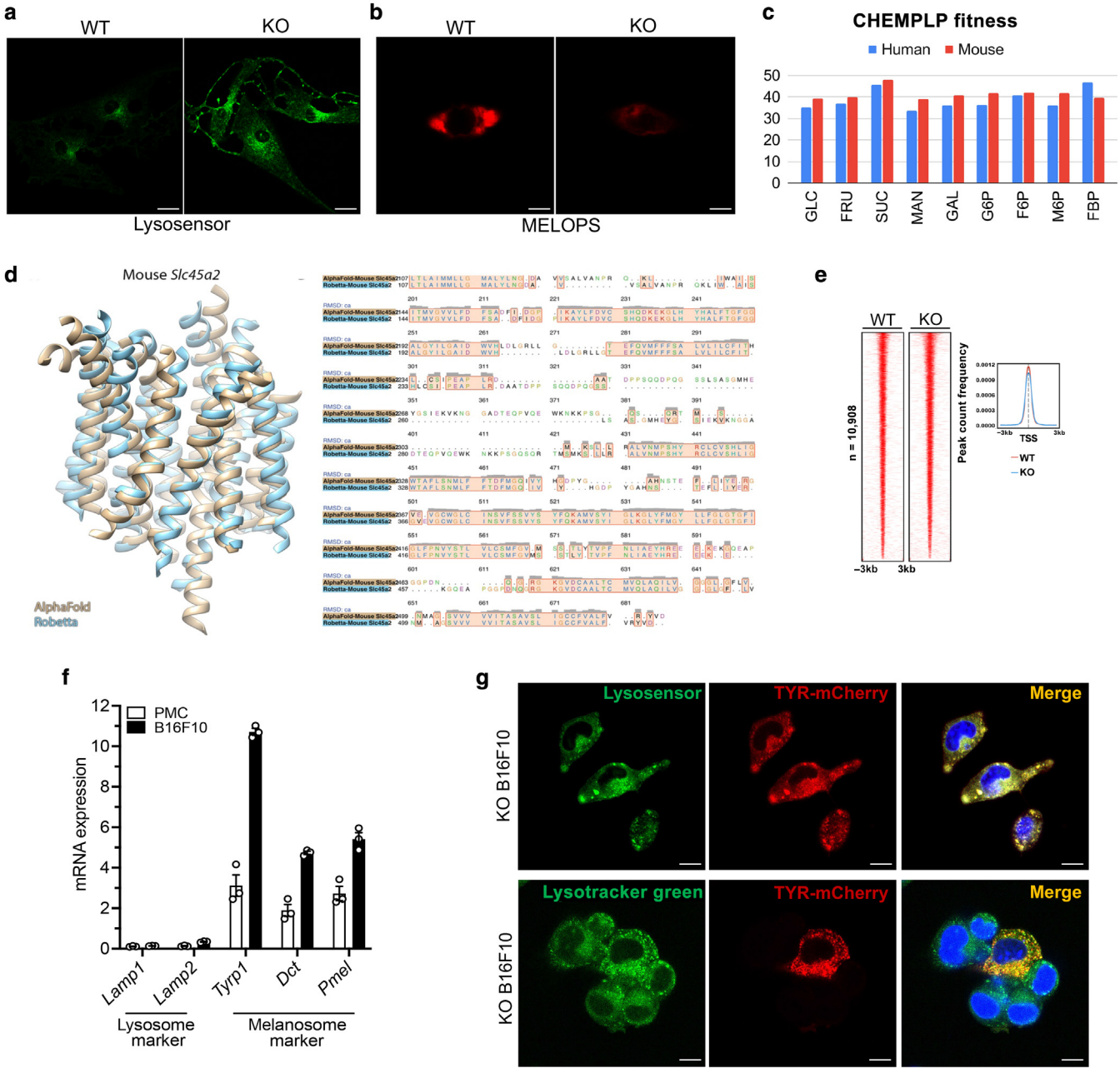

Supplementary Figure S3. Melanosomal pH measurement and sugar-binding docking model of SLC45A2 protein. **(a)** Confocal microscopy images of WT and *Slc45a2*-KO melanocytes stained with 1 μM 37 °C prewarmed lysosensor DND-189 pH indicator (lysosensor) for 40 min. Bar = 10 μm. **(b)** Confocal microscopy images of WT and KO B16F10 cells expressing melanosome pH sensor MELOPS plasmid. Bar = 10 μm. **(c)** We docked the sugar molecules GLC, FRU, SUC, MAN, GAL, G6P, F6P, M6P, and FBP to the two SLC45A2 models using GOLD 2020.3.1. The docking poses were scored on the basis of CHEMPLP fitness scores, and the highest docking scores for the best poses are summarized. **(d)** Comparison of predicted structural models of mouse *Slc45a2*. Superposition of mouse *Slc45a2* predicted by AlphaFold (tan) and Robetta (blue) shows largely agreement between both models with respect to the arrangement of the 12-TM helical core (left). Structure-based sequence alignment for mouse *Slc45a2* models predicted by AlphaFold (tan) and Robetta (blue). Structurally equivalent residue positions are highlighted, and the extent of deviation between the models with respect to CA atoms (RMSD) is indicated above each position. Overall RMSD for the 12-TM helix core is 2.3 Å, with most of the differences between the two models arising near the helix termini (right). **(e)** Heatmap of the ATAC-seq peak signals for 10,908 chromatin-accessible sites in WT and KO melanocytes. The average ATAC-seq peak signals are presented in the right panel. **(f)** mRNA expression levels of two lysosome markers (*Lamp1* and *Lamp2*) and three melanosome markers (*Tyrp1*, *Dct,* and *Pmel*) in PMC and B16F10 cells. **(g)** SLC45A2-KO B16F10 cells were transfected with pCMV-C-mCherry-Tyrosinase plasmid (mCherry-Tyr) and stained with either 1 μM Lysosensor DND-189 or Lysotracker Green DND-26 (Lysotracker Green) for 30 min. Bar = 10 μm. 12-TM, 12-transmembrane; ATAC-seq, assay for transposase-accessible chromatin using sequencing; F6P, β-D-fructose-6-phosphate; FBP, β-D-fructose-1, 6-bisphosphate; FRU, β-D-fructose; G6P, α-D-glucose-6-phosphate; GAL, β-D-galactose; GLC, α-D-glucose; kb, kilobase; KO, knockout; M6P, α-D-mannose-6-phosphate; MAN, α-D-mannose; MELOPS, MELOPS, melanosome-localized pH sensor; min, minute; PMC, primary melanocyte; RMSD, root mean square deviation; SUC, D-sucrose; TSS, transcription start site; WT, wild type.

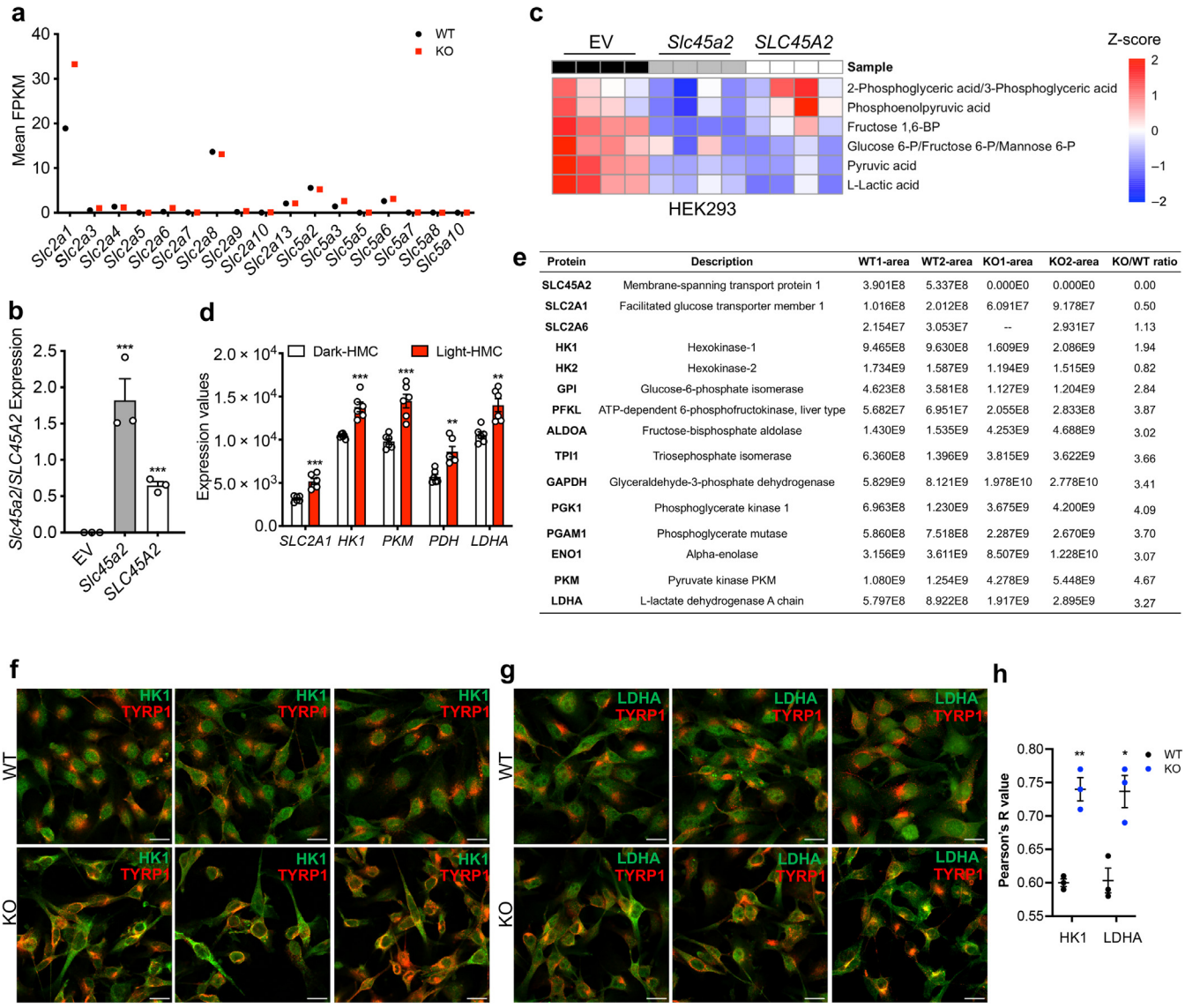

Protein	Description	WT1-area	WT2-area	KO1-area	KO2-area	KO/WT ratio
SLC45A2	Membrane-spanning transport protein 1	3.901E8	5.337E8	0.000E0	0.000E0	0.00
SLC2A1	Facilitated glucose transporter member 1	1.016E8	2.012E8	6.091E7	9.178E7	0.50
SLC2A6		2.154E7	3.053E7	--	2.931E7	1.13
HK1	Hexokinase-1	9.465E8	9.630E8	1.609E9	2.086E9	1.94
HK2	Hexokinase-2	1.734E9	1.587E9	1.194E9	1.515E9	0.82
GPI	Glucose-6-phosphate isomerase	4.623E8	3.581E8	1.127E9	1.204E9	2.84
PFKL	ATP-dependent 6-phosphofructokinase, liver type	5.682E7	6.951E7	2.055E8	2.833E8	3.87
ALDOA	Fructose-bisphosphate aldolase	1.430E9	1.535E9	4.253E9	4.688E9	3.02
TPI1	Triosephosphate isomerase	6.360E8	1.396E9	3.815E9	3.622E9	3.66
GAPDH	Glyceraldehyde-3-phosphate dehydrogenase	5.829E9	8.121E9	1.978E10	2.778E10	3.41
PGK1	Phosphoglycerate kinase 1	6.963E8	1.230E9	3.675E9	4.200E9	4.09
PGAM1	Phosphoglycerate mutase	5.860E8	7.518E8	2.287E9	2.670E9	3.70
ENO1	Alpha-enolase	3.156E9	3.611E9	8.507E9	1.228E10	3.07
PKM	Pyruvate kinase PKM	1.080E9	1.254E9	4.278E9	5.448E9	4.67
LDHA	L-lactate dehydrogenase A chain	5.797E8	8.922E8	1.917E9	2.895E9	3.27

Supplementary Figure S4. *Slc45a2* mediates glycolysis metabolites and enzymes. **(a)** Mean FPKM values from RNA-seq data of SLC2 and SLC5 families in WT and *Slc45a2*-KO PMCs. **(b)** HEK293F cells stably overexpressing EV transfected control, mouse SLC45A2 (*Slc45a2*), and human SLC45A2 (*SLC45A2*) were established (n = 3). **(c)** Heatmap depicts the abundances of glycolytic intermediates of LC−MS–based untargeted metabolomics in HEK293 EV, HEK293 *Slc45a2*, and HEK293 *SLC45A2* cells (n = 4). **(d)** Analysis of GEO datasets (GSE21565) using GEO2R, showing the mRNA expression levels for *SLC2A1*, *HK1*, *PKM*, *PDH*, and *LDHA* from Dark-HMCs and Light-HMCs. **(e)** LC−MS/MS–based proteomics showing the protein abundances (represented by peak areas) of SLC45A2 and glycolysis-related proteins in isolated WT and KO melanosomes. **(f, g)** Immunofluorescence assay was used on WT and KO B16F10 cells; the red signal represents melanosomal marker TYRP1, and the green signal represents HK1 and LDHA. Bar = 20 μm. **(h)** Pearson's correlation (Pearson's R value) was used to quantify the degree of colocalization between HK1 and TYRP1, LDHA, and TYRP1 from three different samples. Data are shown as mean ± SEM. For **b**, **d**, and **h**, Student's *t*-tests were used for the indicated comparisons. $*P < 0.05$, $**P < 0.01$, and $***P < 0.001$. Dark-HMC, dark human melanocyte; EV, empty vector; FPKM, fragments per kilobase of exon per million fragments mapped; GEO, Gene Expression Omnibus; HEK, human embryonic kidney; HK, hexokinase; KO, knockout; LC−MS, liquid chromatography−mass spectrometry; LC−MS/MS, liquid chromatography with tandem mass spectrometry; LDHA, lactate dehydrogenase A; Light-HMC, light human melanocyte; PMC, primary melanocyte; RNA-seq, RNA-sequencing; WT, wild type.

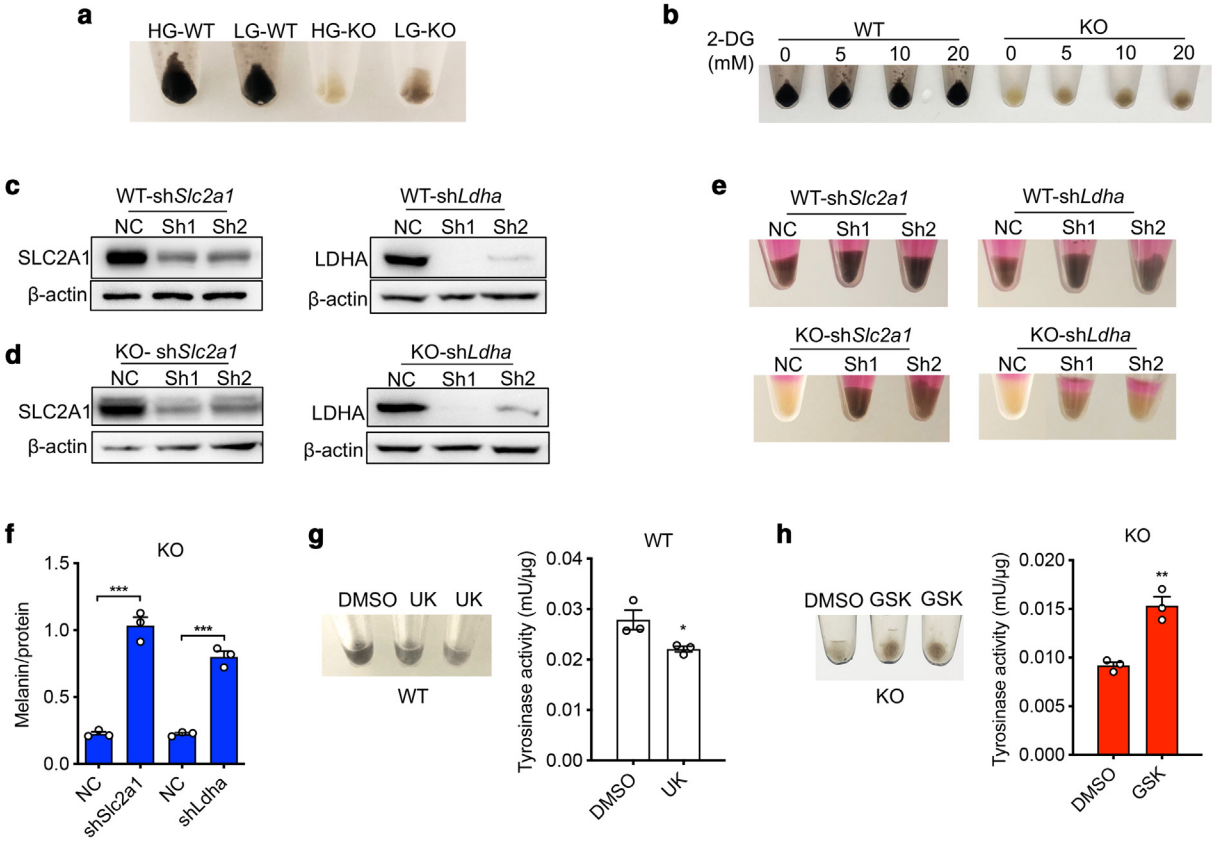

Supplementary Figure S5. The relationship between glycolysis pathway and melanogenesis. **(a)** Cell pellets of WT and KO B16F10 cells under HG and LG conditions. **(b)** Melanin content of WT and KO cell pellets treated with different concentrations of glycolysis inhibitor 2-DG for 12 hours. **(c, d)** shRNA knockdown of NC, *Slc2a1* (sh1, sh2), and *Ldha* (sh1, sh2) in WT and KO B16F10 cells. **(e)** Cell pellets of sh*Slc2a1* and sh*Ldha* WT and KO B16F10 cells. **(f)** Melanin content measurement for NC, sh*Slc2a1*, and sh*Ldha* cells (n = 3). **(g)** Cell pellets and tyrosinase activity of *Slc45a2* WT PMC treated with DMSO and 50 μM UK for 48 hours (n = 3). **(h)** Cell pellets and tyrosinase activity of *Slc45a2* KO PMC treated with DMSO and 10 μM GSK2837808A for 48 hours (n = 3). For **f**, **g**, and **h**, Student's *t*-tests were performed for the indicated comparisons. $^{*}P < 0.05$, $^{**}P < 0.01$, and $^{***}P < 0.001$). 2-DG, 2-deoxy-D-glucose; GSK, GSK2837808A; HG, high glucose; KO, knockout; LG, low glucose; NC, nontargeting control; PMC, primary melanocyte; sh1, shRNA1; sh2, shRNA2; sh*Ldha,* short-hairpin RNA targeting *Ldha;* shRNA, short-hairpin RNA; sh*Slc2a1*, short-hairpin RNA targeting *Slc2a1;* UK, UK5099; WT, wild type.

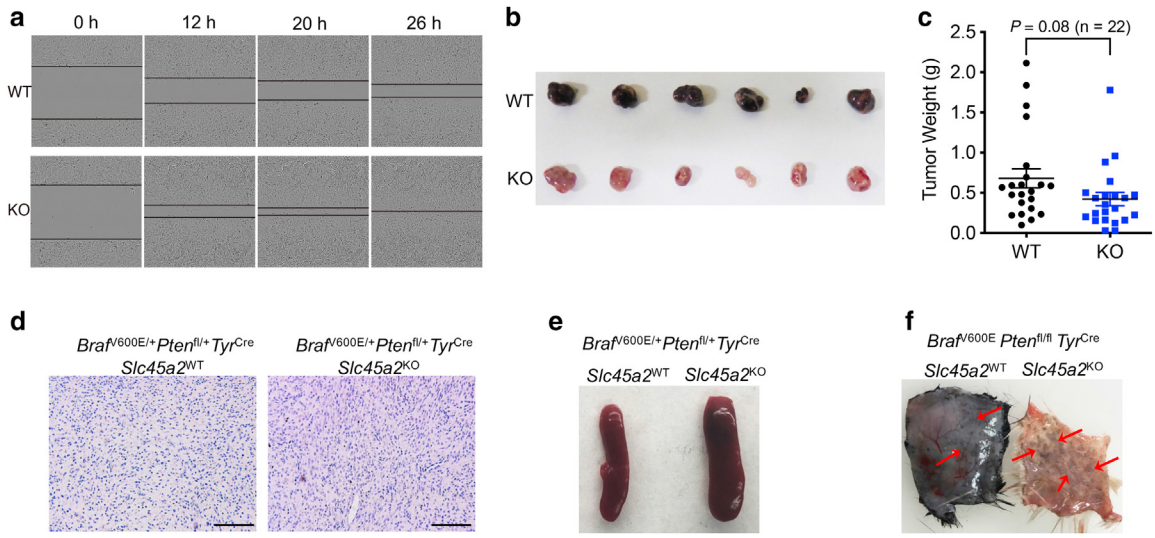

Supplementary Figure S6. The effect of *Slc45a2* deficiency on melanoma proliferation, migration, and *Braf/Pten/Tyr*^{cre} melanoma model. **(a)** Representative images of wound healing assay performed on WT and KO B16F10 cells at different time points (repeated three times). **(b)** Subcutaneous tumor separated from nude mice injected with WT and *Slc45a2*-KO B16F10 cells. **(c)** The weight of WT and *Slc45a2*-KO subcutaneous tumor (n = 22). **(d)** *Braf*$^{V600E/+}$*pten*$^{fl/fl}$*Tyr*^{Cre} *Slc45a2*^{WT} and *Braf*$^{V600E/+}$*Pten*$^{fl/fl}$*Tyr*^{Cre} *Slc45a2*^{KO} mice were euthanized, and tumor specimens were prepared for staining with H&E. Bar = 100 μm. **(e)** Representative images of spleens from mice bearing *Braf*$^{V600E/+}$*pten*$^{fl/fl}$*Tyr*^{Cre} *Slc45a2*^{WT} and *Braf*$^{V600E/+}$*Pten*$^{fl/fl}$*Tyr*^{Cre} *Slc45a2*^{KO} tumors. **(f)** Skin specimen separated from WT and *Slc45a2*-KO mice bred with *Braf*^{V600E}*Pten*$^{fl/fl}$*Tyr*^{Cre} metastatic melanoma model. For **c**, Student's *t*-tests were performed for the indicated comparisons. $*P < 0.05$, $**P < 0.01$, and $***P < 0.001$. h, hour; KO, knockout; WT, wild type.